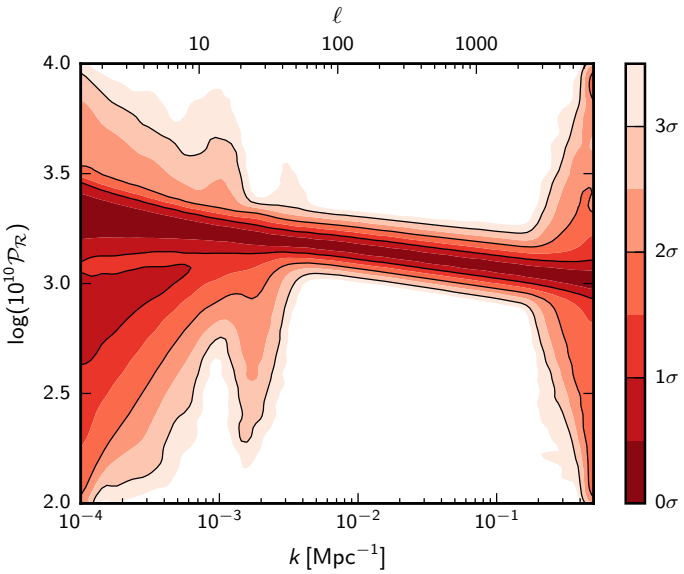

Fig. 26. Bayesian reconstruction of the primordial power spectrum averaged over different values of $N_{\rm int}$ (as shown in Fig. 24), weighted according to the Bayesian evidence. The region $30 < \ell < 2300$ is highly constrained, but the resolution is lacking to say anything precise about higher ℓ. At lower ℓ, cosmic variance reduces our knowledge of $\mathcal{P}_{\mathcal{R}}(k)$. The weights assigned to the lower $N_{\rm int}$ models outweigh those of the higher models, so no oscillatory features are visible here.

prior. Including these ancillary likelihoods improves the constraint on the PPS by helping to fix the cosmological parameters (e.g., H_0, τ, and the late-time expansion history), which in this context may be regarded as nuisance parameters. These results were obtained by modifying `CosmoMC` to incorporate the n-knot parameterization of the PPS. Here 12 knots were used and the mean reconstruction as well as the 1σ and 2σ limits are shown. Some 1σ sample trajectories (dashed curves) are also shown to illustrate the degree of correlation or smoothing of the reconstruction. The tensor trajectories are also shown, but, as explained above, have been constrained to be straight lines. In the top panel r is allowed to freely float, and a wide range of r is allowed because of the near-degeneracy with the low-k scalar power. Two illustrative values of fixed r (i.e., $r = 0.1$ and $r = 0.01$) are also shown to give an idea of how much the reconstruction is sensitive to variations in r within the range of presently plausible values.

The reconstructions using the 2013 *Planck* likelihood in place of the 2015 likelihood are broadly consistent with the reconstruction shown in Fig. 27. To demonstrate robustness with respect to the interpolation scheme we tried using linear interpolation instead of cubic splines and found that the reconstruction was consistent provided enough knots (i.e., $n_{\rm knot} \approx 14$) were used. At intermediate k the reconstruction is consistent with a simple power law, corresponding to a straight line in Fig. 27. We observe that once k drops, so that the effective multipole being probed is below about 60, deviations from a power law appear, but the dispersion in allowed trajectories also rises as a consequence of cosmic variance. The power deficit at $k \approx 0.002\,{\rm Mpc}^{-1}$ (i.e., $\ell_k \equiv kD_{\rm rec} \approx 30$, where $D_{\rm rec}$ is the comoving distance to recombination) is largely driven by the power spectrum anomaly in the $\ell \approx 20$–30 range that has been evident since the early spectra from WMAP (Bennett et al. 2011), and verified by *Planck*.

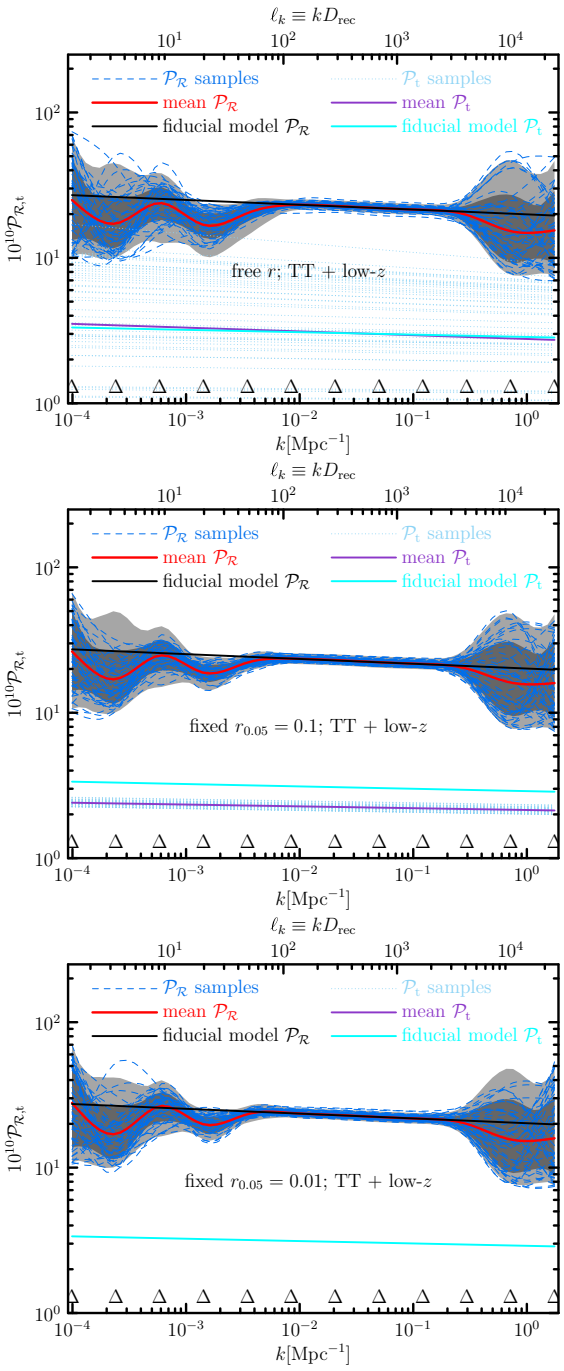

Fig. 27. Reconstructed power spectra applied to the *Planck* 2015 data using 12 knots (with positions marked as Δ at the bottom of each panel) with cubic spline interpolation. Mean spectra as well as sample trajectories are shown for scalars and tensors, and $\pm1\sigma$ and $\pm2\sigma$ limits are shown for the scalars. The fiducial tensor spectrum corresponds, arbitrarily, to $r = 0.13$. *Top*: uniform prior, $0 \le r \le 1$. *Middle*: fixed, $r = 0.1$. *Bottom*: fixed, $r = 0.01$. Data sets: *Planck* TT+lowP+BAO+SN+HST+$z_{\rm re} > 6$ prior. $D_{\rm rec}$ is the comoving distance to recombination.

We also explore the impact of including the *Planck* polarization likelihood in the reconstruction. Figure 28 shows the reconstructed power spectra using various combinations of the polarization and temperature data. The $\ell < 30$ treatments are the same in all cases, so this is mainly a test of the higher k region. What is seen is that, except at high k, the *EE* polarization data also enforce a nearly uniform $n_{\rm s}$, consistent with that

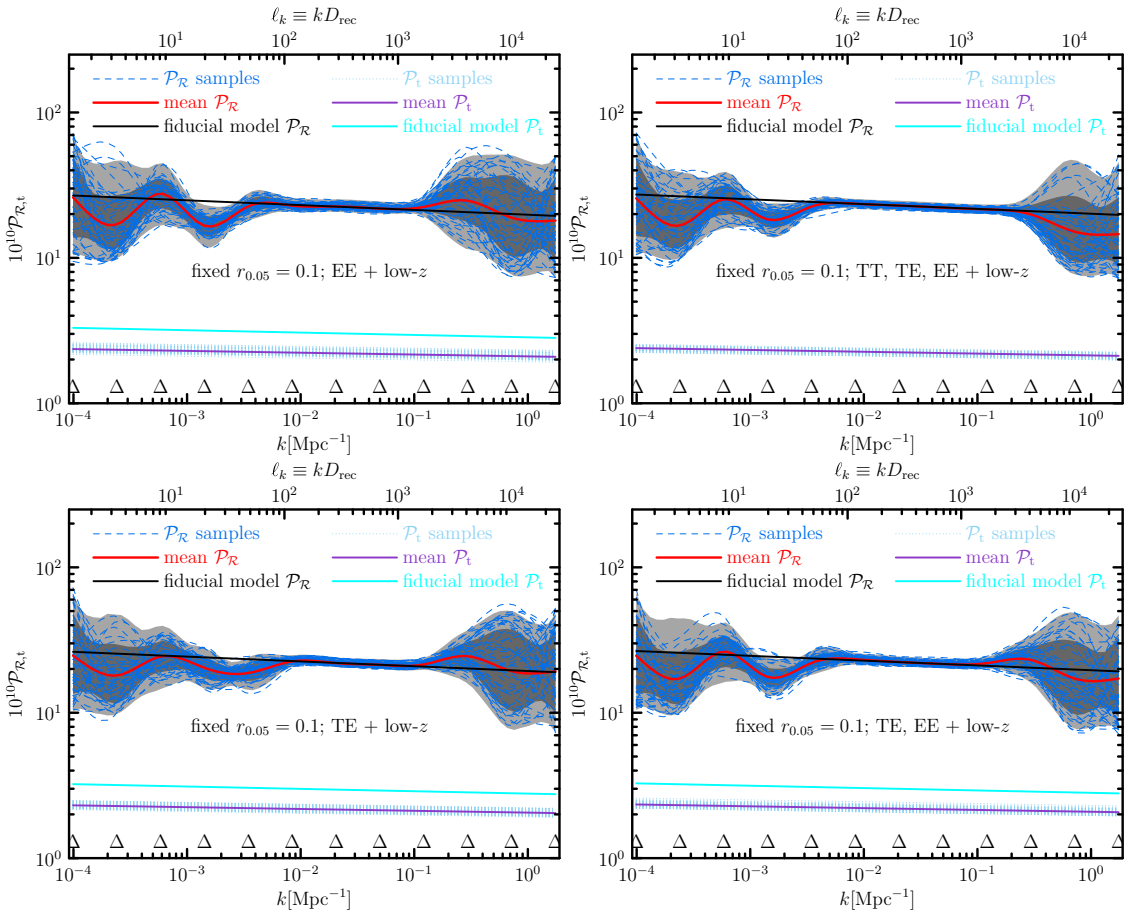

Fig. 28. Reconstructed 12-knot power spectra with polarization included. Data sets in common: lowT+lowP+BAO+SN+HST+$z_{\rm re} > 6$ prior.

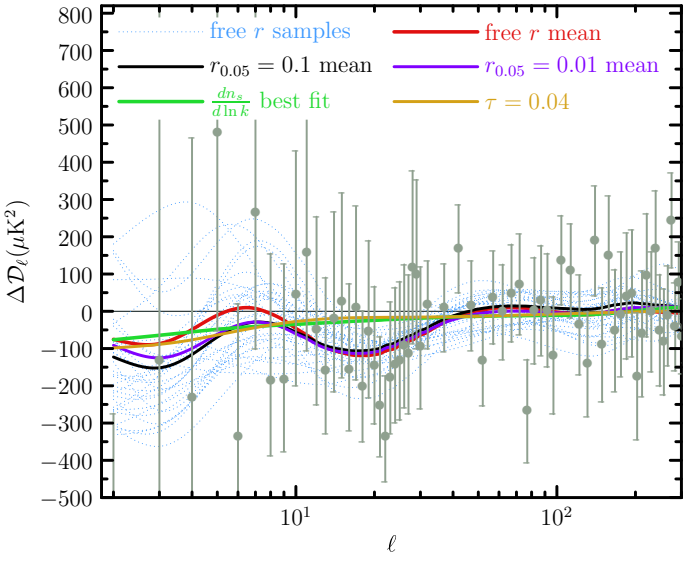

Fig. 29. Reconstructed $\mathcal{D}_\ell^{\rm TT}$ power spectra with the base ΛCDM best fit subtracted. The mean spectra shown are for the floating r and the two fixed r cases with 12 cubic spline knots. These should be contrasted with the running best-fit mean (green) and the similar looking uniform $n_{\rm s}$ case in which τ has been lowered from its best-fit base ΛCDM value to 0.04. Data points are the *Planck* 2015 `Commander` ($\ell < 30$) and `Plik` ($\ell \geq 30$) temperature power spectrum.

from *TT*, over a broad k-range. When *TE* is used alone, or *TE* and *EE* are used in combination, the result is also very similar. The upper right panel shows the constraints from all three spectra together, and the errors on the reconstruction are now better than those from *TT* alone.

It is interesting to examine how the *TT* power spectrum obtained using the above reconstructions compares to the CMB data, in particular around the range $\ell \approx 20$–30, corresponding roughly to $k_4 \approx 1.5 \times 10^{-3}\,{\rm Mpc}^{-1}$. In Fig. 29 the differences in $\mathcal{D}_\ell^{\rm TT}$ from the best-fit simple power-law model are plotted for various assumptions concerning r. We see that a better fit than the power-law model can apparently be obtained around $\ell \approx 20$–30. We quantify this improvement below.

Due to the degeneracy of scalar and tensor contributions to $\mathcal{D}_\ell^{TT}$, the significance of the low-ℓ anomaly depends on the tensor prior and whether polarization data are used. For $k < 10^{-3}\,{\rm Mpc}^{-1}$, once more degeneracy appears: the shape of $\mathcal{D}_\ell^{TT}$ also depends on the reionization optical depth, τ. In Fig. 29 we also show the effect of replacing the best-fit τ for tilted base ΛCDM with a low value, while keeping $A_{\rm s}{\rm e}^{-2\tau}$ unchanged. A low τ bends $\mathcal{D}_\ell^{\rm TT}$ downward at $\ell \lesssim 10$. For the 12-knot (or similar) runs, if τ is allowed to run into the (nonphysically) small values $\tau \lesssim 0.04$, a slight rise in $\mathcal{P}_\mathcal{R}(k)$ at $k \approx 3 \times 10^{-4}\,{\rm Mpc}^{-1}$ is preferred to compensate the low-τ effect. This degeneracy can be broken to a certain extent using low-redshift data: $z_{\rm re} > 6$ from quasar observations (Becker et al. 2001), BAO (SDSS), Supernova (JLA), and HST.

It is evident that allowing $n_{\rm s}$ to run is not what the $\mathcal{D}_\ell^{TT}$ data prefer. The best-fit running is also shown in Fig. 29. The k-space $\mathcal{P}_\mathcal{R}(k)$-response in Fig. 27 shows that running does not capture the shape of the low-ℓ residuals.

Table 11. Reduced χ^2 and p-values for low-k knots (5 knots) and high-k knots (6 knots, pivot knot excluded), with the null hypothesis being the best-fit power-law spectrum.

r prior	low-z data	*Planck* data	low-k $\chi^2_{\rm reduced}$	low-k p-value	high-k $\chi^2_{\rm reduced}$	high-k p-value	q_3 constraint	q_4 constraint
$0 \le r \le 1$	used	TT	0.95	0.45	0.17	0.98	-0.07 ± 0.28	-0.39 ± 0.20
$r = 0.01$	used	TT	1.13	0.34	0.09	0.997	0.01 ± 0.24	-0.23 ± 0.12
$r = 0.01$	not used	TT	0.89	0.49	0.36	0.90	0.10 ± 0.24	-0.23 ± 0.12
$r = 0.1$	used	TT	1.70	0.13	0.12	0.994	-0.04 ± 0.26	-0.28 ± 0.13
$r = 0.1$	not used	TT	1.46	0.20	0.38	0.89	0.05 ± 0.27	-0.28 ± 0.13
$r = 0.1$	used	TT, TE, EE	1.71	0.13	0.17	0.985	-0.02 ± 0.25	-0.30 ± 0.12
$r = 0.1$	used	TE, EE	1.72	0.13	0.38	0.89	0.06 ± 0.25	-0.32 ± 0.15
$r = 0.1$	used	TE	1.80	0.11	0.26	0.95	-0.02 ± 0.27	-0.17 ± 0.16
$r = 0.1$	used	EE	1.78	0.11	0.18	0.98	0.09 ± 0.25	-0.39 ± 0.16
$r = 0.1$	used	TT+lensing	1.54	0.17	0.05	0.9995	0.05 ± 0.25	-0.27 ± 0.13

Notes. Low-z data refers to BAO+SN+HST+$z_{\rm re} > 6$ prior. In all cases lowP data are used.

We have shown that the cubic spline reconstruction studied in this section consistently produces a dip in q_4, corresponding to $k \approx 1.5 \times 10^{-3}\,{\rm Mpc}^{-1}$. We now turn to the question of whether this result is real or simply the result of cosmic variance. To assess the statistical significance of the departures of the mean reconstruction from a simple power law, we calculate the low-k and high-k reduced χ^2 for the five q_b values for scales below and six q_b values ($b \neq p$) for scales above $50/D_{\rm rec}$, respectively, indicating the corresponding p-values (i.e., probability to exceed), for various data combinations, in Table 11. The high-k fit is better than expected for reasons that we do not understand, but we attribute this situation to chance. The low-k region shows a poor fit, but in no case does the p-value fall below 10%. Therefore, even though the low-k dip is robust against the various choices made for the reconstruction, we conclude that it is not statistically significant. The plot for the knot position of the dip (corresponding to q_4) in Fig. 30 does not contradict this conclusion.

Because of the r degeneracy associated with the scalar power, it is best when quoting statistics to use the fixed r cases, although for completeness we show the floating r case as well. There is also a smaller effect associated with the τ degeneracy, and the values quoted have restricted the redshift of reionization to exceed 6. The value $z_{\rm re} = 6.5$ was used in Planck Collaboration XIII (2016). The significance of the low-k anomaly is meaningful only if an explicit r prior and low-redshift constraint on τ have been applied.

Finally, we relate the reconstructed $\mathcal{P}_{\mathcal{R}}(k)$ calculated above to the trajectories of the slow-roll parameter $\epsilon = -\dot{H}/H^2|_{k=aH}$ plotted as a function of k (see Fig. 31). We also plot in Fig. 32 the reconstructed inflationary potential in the region over which the inflationary potential is constrained by the data. Here canonical single-field inflation is assumed, and the value of r enters solely to fix the height of the potential at the pivot scale. This is not entirely self-consistent, but justified by the lack of constraining power on the tensors at present.

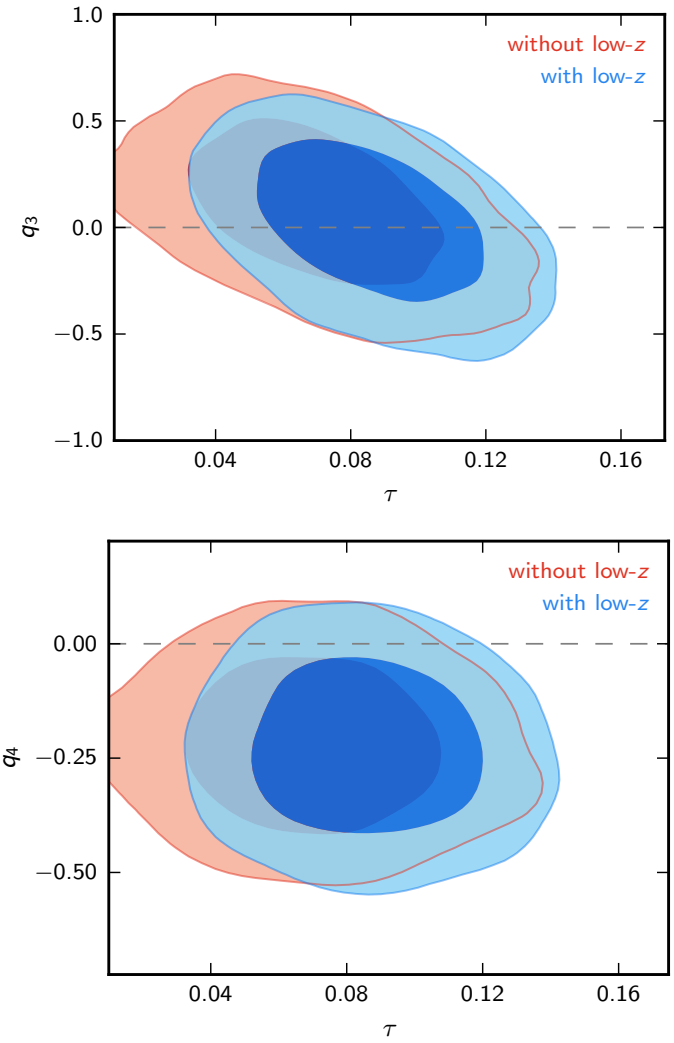

Fig. 30. The degeneracy between τ and the knot variables q_3 and q_4 in the 12-knot case shown in Fig. 27.

8.4. Power spectrum reconstruction summary

The three non-parametric methods for reconstructing the primordial power spectrum explored here support the following two conclusions:

1. Except possibly at low k, over the range of k where the CMB data best constrain the form of the primordial power spectrum, none of the three methods finds any statistically significant evidence for deviations from a simple power-law form. The fluctuations seen in this regime are entirely consistent with the expectations from cosmic variance and noise.
2. At low k, all three methods reconstruct a power deficit at $k \approx 1.5$–$2.0 \times 10^{-3}\,{\rm Mpc}^{-1}$, which can be linked to the dip in the TT angular power spectrum at $\ell \approx 20$–30. This

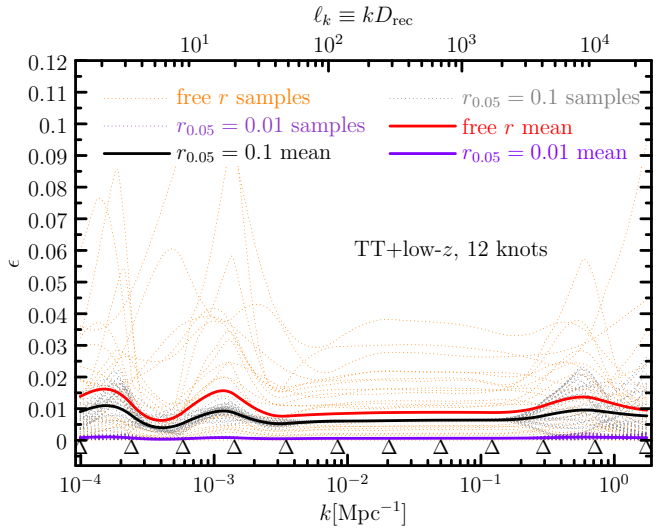

Fig. 31. Slow-roll parameter ϵ for reconstructed trajectories using 12 knots (marked as Δ at the bottom of the figure) with cubic spline interpolation. The mean values are shown for floating r and r fixed to be 0.1 and 0.01. Sample 1σ trajectories shown for the floating r case show wide variability, which is significantly diminished if r is fixed to $r = 0.1$, as shown.

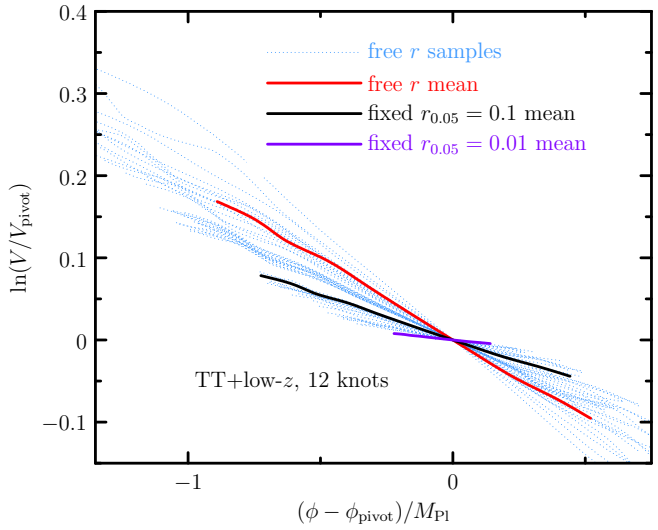

Fig. 32. Reconstructed single-field inflaton potentials from the cubic spline power spectra mode expansion using 12 knots.

agreement suggests that the reconstruction of this "anomaly" is not an artefact of any of the methods, but rather inherent in the CMB data themselves. However, the evidence for this feature is marginal since it is in a region of the spectrum where the fluctuations from cosmic variance are large.

3. We have verified that the power deficit at $\ell = 20$–30 is not substantially modified (a) by removing from the CMB pattern the hottest and coldest peaks selected by the Kolmogorov-Smirnov test studied in Sects. 4.5.3 and 4.5.4 of Planck Collaboration XVI (2016) or (b) by substituting the anomalously cold region around the Cold Spot with Gaussian constrained realizations.

9. Search for parameterized features

In this section, we explore the possibility of a radical departure from the near-scale-invariant power-law spectrum $\mathcal{P}^0_{\mathcal{R}}(k) = A_{\rm s}(k/k_*)^{n_{\rm s}-1}$ of the standard slow-roll scenario for a selection of theoretically motivated parameterizations of the spectrum (see Chluba et al. 2015 for a recent review).

9.1. Models

9.1.1. Step in the inflaton potential

A sudden, step-like feature in the inflaton potential (Adams et al. 2001) or the sound speed (Achúcarro et al. 2011) leads to a localized oscillatory burst in the scalar primordial power spectrum. A general parameterization describing both a tanh-step in the potential and in the warp term of a DBI model was proposed in Miranda & Hu (2014):

$$\ln \mathcal{P}^{\rm s}_{\mathcal{R}}(k) = \exp\left[\ln \mathcal{P}^0_{\mathcal{R}}(k) + \mathcal{I}_0(k) + \ln\left(1 + \mathcal{I}_1^2(k)\right)\right], \tag{71}$$

where the first- and second-order terms are given by

$$\mathcal{I}_0 = \left[\mathcal{A}_{\rm s}\,\mathcal{W}_1^{(0)}(k/k_{\rm s}) + \mathcal{A}_2\,\mathcal{W}_2^{(0)}(k/k_{\rm s}) + \mathcal{A}_3\,\mathcal{W}_3^{(0)}(k/k_{\rm s})\right]\mathcal{D}\left(\frac{k/k_{\rm s}}{x_{\rm s}}\right), \tag{72}$$

$$\mathcal{I}_1 = \frac{1}{\sqrt{2}}\left\{\frac{\pi}{2}(1-n_{\rm s}) + \left[\mathcal{A}_{\rm s}\,\mathcal{W}_1^{(1)}(k/k_{\rm s}) + \mathcal{A}_2\,\mathcal{W}_2^{(1)}(k/k_{\rm s}) + \mathcal{A}_3\,\mathcal{W}_3^{(1)}(k/k_{\rm s})\right]\mathcal{D}\left(\frac{k/k_{\rm s}}{x_{\rm s}}\right)\right\}, \tag{73}$$

with window functions

$$\mathcal{W}_1^{(0)}(x) = \frac{1}{2x^3}\left[\left(18x - 6x^3\right)\cos 2x + \left(15x^2 - 9\right)\sin 2x\right], \tag{74}$$

$$\mathcal{W}_2^{(0)}(x) = \frac{3}{2x^3}\left[\sin(2x) - 2x\cos(2x) - x^2\sin(2x)\right], \tag{75}$$

$$\mathcal{W}_3^{(0)}(x) = \frac{1}{x^3}\left[6x\cos(2x) + (4x^2 - 3)\sin(2x)\right], \tag{76}$$

$$\mathcal{W}_1^{(1)}(x) = -\frac{1}{x^3}\left\{3(x\cos x - \sin x)\left[3x\cos x + \left(2x^2 - 3\right)\sin x\right]\right\}, \tag{77}$$

$$\mathcal{W}_2^{(1)}(x) = \frac{3}{x^3}(\sin x - x\cos x)^2, \tag{78}$$

$$\mathcal{W}_3^{(1)}(x) = -\frac{1}{x^3}\left[3 + 2x^2 - \left(3 - 4x^2\right)\cos(2x) - 6x\sin(2x)\right], \tag{79}$$

and damping function

$$\mathcal{D}(x) = \frac{x}{\sinh x}\cdot \tag{80}$$

Due to the high complexity of this model, we focus on the limiting case of a step in the potential ($\mathcal{A}_2 = \mathcal{A}_3 = 0$).

9.1.2. Logarithmic oscillations

Logarithmic modulations of the primordial power spectrum generically appear, for example, in models with non-Bunch-Davies initial conditions (Martin & Brandenberger 2001; Danielsson 2002; Bozza et al. 2003), or, approximately, in the axion monodromy model, explored in more detail in Sect. 10. We assume a constant modulation amplitude and use

$$\mathcal{P}^{\rm log}_{\mathcal{R}}(k) = \mathcal{P}^0_{\mathcal{R}}(k)\left\{1 + \mathcal{A}_{\rm log}\cos\left[\omega_{\rm log}\ln\left(\frac{k}{k_*}\right) + \varphi_{\rm log}\right]\right\}. \tag{81}$$

Table 12. Parameters and prior ranges.

Model	Parameter	Prior range
Step	$\mathcal{A}_s$	$[0, 2]$
	$\log_{10}\left(k_s/\mathrm{Mpc}^{-1}\right)$	$[-5, 0]$
	$\ln x_s$	$[-1, 5]$
Log osc.	$\mathcal{A}_{\log}$	$[0, 0.5]$
	$\log_{10}\omega_{\log}$	$[0, 2.1]$
	$\varphi_{\log}$	$[0, 2\pi]$
Linear osc.	$\mathcal{A}_{\rm lin}$	$[0, 0.5]$
	$\log_{10}\omega_{\rm lin}$	$[0, 2]$
	$n_{\rm lin}$	$[-1, 1]$
	$\varphi_{\rm lin}$	$[0, 2\pi]$
Cutoff	$\log_{10}\left(k_c/\mathrm{Mpc}^{-1}\right)$	$[-5, -2]$

9.1.3. Linear oscillations

A modulation linear in k can be obtained, for example, in boundary effective field theory models (Jackson & Shiu 2013), and is typically accompanied by a scale-dependent modulation amplitude. We adopt the parameterization used in Meerburg & Spergel (2014), which allows for a strong scale dependence of the modulation amplitude:

$$\mathcal{P}^{\rm lin}_{\mathcal{R}}(k) = \mathcal{P}^{0}_{\mathcal{R}}(k)\left[1 + \mathcal{A}_{\rm lin}\left(\frac{k}{k_*}\right)^{n_{\rm lin}}\cos\left(\omega_{\rm lin}\frac{k}{k_*} + \varphi_{\rm lin}\right)\right]. \quad (82)$$

9.1.4. Cutoff model

If today's largest observable scales exited the Hubble radius before the inflaton field reached the slow-roll attractor, the amplitude of the primordial power spectrum is typically strongly suppressed at low k. As an example of such a model, we consider a scenario in which slow roll is preceded by a stage of kinetic energy domination. The resulting power spectrum was derived by Contaldi et al. (2003) and can be expressed as

$$\ln\mathcal{P}^{\rm c}_{\mathcal{R}}(k) = \ln\mathcal{P}^{0}_{\mathcal{R}}(k) + \ln\left(\frac{\pi}{16}\frac{k}{k_c}|C_c - D_c|^2\right), \quad (83)$$

with

$$C_c = \exp\left(\frac{-ik}{k_c}\right)\left[H_0^{(2)}\left(\frac{k}{2k_c}\right) - \left(\frac{k_c}{k} + i\right)H_1^{(2)}\left(\frac{k}{2k_c}\right)\right], \quad (84)$$

$$D_c = \exp\left(\frac{ik}{k_c}\right)\left[H_0^{(2)}\left(\frac{k}{2k_c}\right) - \left(\frac{k_c}{k} - i\right)H_1^{(2)}\left(\frac{k}{2k_c}\right)\right], \quad (85)$$

where $H_n^{(2)}$ denotes the Hankel function of the second kind. The power spectrum in this model is exponentially suppressed for wavenumbers smaller than the cutoff scale k_c and converges to a standard power-law spectrum for $k \gg k_c$, with an oscillatory transition region for $k \gtrsim k_c$.

9.2. Analysis and results

We use `MultiNest` to evaluate the Bayesian evidence for the models, establish parameter constraints, and roughly identify the global maximum likelihood region of parameter space. The features model best-fit parameters and $\ln\mathcal{L}$ are then obtained with the help of the `CosmoMC` minimization algorithm taking narrow priors around the `MultiNest` best fit. We assign flat prior probabilities to the parameters of the features models with prior ranges listed in Table 12. Note that throughout this section for the sake of maximizing sensitivity to very sharp features, the unbinned ("bin1") versions of the high-ℓ TT and TT, TE, EE likelihoods are used instead of the standard binned versions.

Table 13. Improvement in fit and Bayes factors with respect to power-law base ΛCDM for *Planck* TT+lowP and *Planck* TT, TE, EE+lowP data, as well as approximate probability to exceed the observed $\Delta\chi^2$ (p-value), constructed from simulated *Planck* TT+lowP data.

Model	*Planck* TT+lowP		*Planck* TT, TE, EE+lowP		PTE
	$\Delta\chi^2$	$\ln B$	$\Delta\chi^2$	$\ln B$	
Step	−8.6	−0.3	−7.3	−0.6	0.09
Log osc.	−10.6	−1.9	−10.1	−1.5	0.24
Linear osc.	−8.9	−1.9	−10.9	−1.3	0.50
Cutoff	−2.0	−0.4	−2.2	−0.6	0.12

Notes. Negative Bayes factors indicate a preference for the power-law model.

Since the features considered here can lead to broad distortions of the CMB angular power spectrum degenerate with the late time cosmological parameters (Miranda & Hu 2014), in all cases we simultaneously vary primordial parameters and all the ΛCDM parameters, but keep the foreground parameters fixed to their best-fit values for the power-law base ΛCDM model.

We present the Bayes factors with respect to the power-law base ΛCDM model and the improvement in the effective χ^2 over the power-law model in Table 13. For our choice of priors, none of the features models is preferred over a power-law spectrum. The best-fit power spectra are plotted in Fig. 33. While the cutoff and step model best fits reproduce the large-scale suppression at $\ell \approx 20$–30 also obtained by direct power spectrum reconstruction in Sect. 8, the oscillation models prefer relatively high frequencies beyond the resolution of the reconstruction methods.

In addition to the four features models we also show in Fig. 33 the best fit of a model allowing for steps in both inflaton potential and warp (brown line). Note the strong resemblance to the reconstructed features of the previous section. The effective $\Delta\chi^2$ for this model is −12.1 (−11.5) for *Planck* TT+lowP (*Planck* TT, TE, EE+lowP) data at the cost of adding five new parameters, resulting in a ln-Bayes factor of −0.8 (−0.4). A similar phenomenology can be also be found for a model with a sudden change in the slope of the inflaton potential (Starobinsky 1992; Choe et al. 2004), which yields a best-fit $\Delta\chi^2 = -4.5$ (−4.9) for two extra parameters.

As shown in Table 14, constraints on the remaining cosmological parameters are not significantly affected when allowing for the presence of features.

For the cutoff and step models, the inclusion of *Planck* small-scale polarization data does not add much in terms of direct sensitivity. The best fits lie in the same parameter region as for *Planck* TT+lowP data, and the $\Delta\chi^2$ and Bayes factors are not subject to major changes. The two oscillation models' *Planck* TT+lowP best fits, on the other hand, also predict a non-negligible signature in the polarization spectra at high ℓ. Therefore, if the features were real, one would expect an additional improvement in $\Delta\chi^2$ for *Planck* TT, TE, EE+lowP. This is not the case here. Though the linear oscillation model's maximum $\Delta\chi^2$ does increase, the local $\Delta\chi^2$ in the *Planck* TT+lowP best-fit regions is in fact reduced for both models, and the global likelihood maxima occur at different frequencies ($\log_{10}\omega_{\log} = 1.25$ and $\log_{10}\omega_{\rm lin} = 1.02$) compared to their *Planck* TT+lowP counterparts.

Table 14. Best-fit features parameters and parameter constraints on the remaining cosmological parameters for the four features models for *Planck* TT+lowP data.

Parameter	Step	Log osc.	Linear osc.	Cutoff	Power law
$100\,\omega_b$	2.23 ± 0.02	2.22 ± 0.02	2.23 ± 0.02	2.23 ± 0.02	2.23 ± 0.02
$10\,\omega_c$	1.20 ± 0.02	1.20 ± 0.02	1.20 ± 0.02	1.19 ± 0.02	1.19 ± 0.02
$100\,\theta_{MC}$	1.0409 ± 0.0004	1.0409 ± 0.0004	1.0409 ± 0.0004	1.0410 ± 0.0005	1.0409 ± 0.0005
τ	0.083 ± 0.015	0.082 ± 0.015	0.084 ± 0.014	0.086 ± 0.017	0.085 ± 0.016
$\ln\left(10^{10} A_s\right)$	3.10 ± 0.03	3.10 ± 0.03	3.10 ± 0.03	3.11 ± 0.03	3.10 ± 0.03
n_s	0.966 ± 0.005	0.970 ± 0.007	0.967 ± 0.004	0.968 ± 0.005	0.968 ± 0.005
$\mathcal{A}_s$	0.374	...	...	...	...
$\log_{10}\left(k_s/\mathrm{Mpc}^{-1}\right)$	−3.10	...	...	...	...
$\ln x_s$	0.342	...	...	...	...
$\mathcal{A}_{log}$	...	0.0278	...	...	...
$\log_{10}\omega_{log}$	...	1.51	...	...	...
$\varphi_{log}/2\pi$	...	0.634	...	...	...
$\mathcal{A}_{lin}$	...	...	0.0292	...	...
$\log_{10}\omega_{lin}$	...	...	1.73	...	...
n_{lin}	...	...	0.662	...	...
$\varphi_{lin}/2\pi$	...	...	0.554	...	...
$\log_{10}\left(k_c/\mathrm{Mpc}^{-1}\right)$	...	...	...	−3.44	...

Notes. The foreground parameters have been fixed to their power-law base ΛCDM best-fit values.

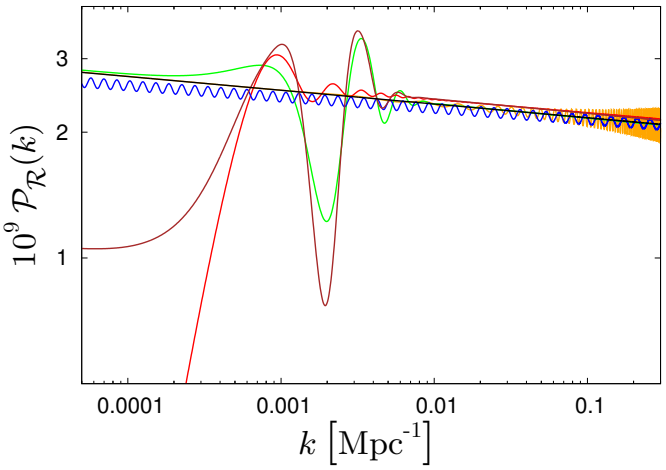

Fig. 33. Best-fit power spectra for the power-law (black curve), step (green), logarithmic oscillation (blue), linear oscillation (orange), and cutoff (red) models using *Planck* TT+lowP data. The brown curve is the best fit for a model with a step in the warp *and* potential (Eqs. (71)−(80)).

In addition to the Bayesian model comparison analysis, we also approach the matter of the statistical relevance of the features models from a frequentist statistics perspective in order to give the $\Delta\chi^2$ numbers a quantitative interpretation. Assuming that the underlying $\mathcal{P}_{\mathcal{R}}(k)$ was actually a featureless power law, we can ask how large an improvement to $\ln\mathcal{L}$ the different features models would yield on average just by overfitting scatter from cosmic variance and noise. For this purpose, we simulate *Planck* power spectrum data sets consisting of temperature and polarization up to $\ell = 29$ and unbinned temperature for $30 \leq \ell \leq 2508$, taking as input fiducial spectra the power-law base ΛCDM model's best-fit spectra.

For each of these simulated *Planck* data sets, we perform the following procedure: (i) find the power-law ΛCDM model's best-fit parameters with `CosmoMC`'s minimization algorithm; (ii) fix the non-primordial parameters ($\omega_b, \omega_c, \theta_{MC}, \tau$) to their respective best-fit values; (iii) using `MultiNest`, find the best fit of the features models;[9] and (iv) extract the effective $\Delta\chi^2$ between power-law and features models.

The resulting distributions are shown in Fig. 34. Compared to the real data $\Delta\chi^2$ values from Table 13, they are biased towards lower values, since we do not vary the late-time cosmological parameters in the analysis of the simulated data. Nonetheless, the observed improvements in the fit do not appear to be extraordinarily large, with the respective (conservative) p-values ranging between 0.09 and 0.50.

These observations lead to the conclusion that even though some of the peculiarities seen in the residuals of the *Planck* data with respect to a power-law primordial spectrum may be explained in terms of primordial features, none of the simple model templates considered here is required by *Planck* data. The simplicity of the power-law spectrum continues to give it an edge over more complicated initial spectra and the most plausible explanation for the apparent features in the data remains that we are just observing fluctuations due to cosmic variance at large scales and noise at small scales.

10. Implications of *Planck* bispectral constraints on inflationary models

The combination of power spectrum constraints and primordial non-Gaussianity (NG) constraints, such as the *Planck* upper bound on the NG amplitude f_{NL} (Planck Collaboration XVII 2016), can be exploited to limit extensions to the simplest standard single-field models of slow-roll inflation. The next subsection considers inflationary models with a non-standard kinetic term (Garriga & Mukhanov 1999), where the inflaton Lagrangian is a general function of the scalar inflaton field and its first derivative, i.e., $\mathfrak{L} = P(\phi, X)$, where $X = -g^{\mu\nu}\partial_\mu\phi\partial_\nu\phi/2$

[9] Due to the multimodal nature of the posterior, usual minimization routines perform poorly here.

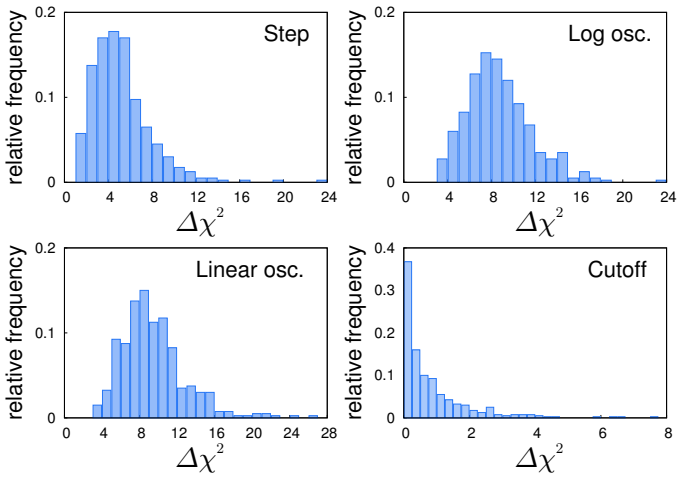

Fig. 34. Distribution of $\Delta\chi^2$ from 400 simulated *Planck* TT+lowP data sets.

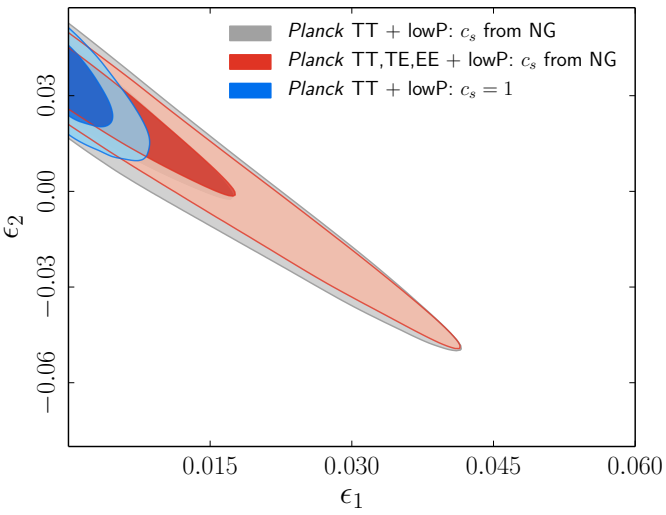

Fig. 35. (ϵ_1, ϵ_2) 68% and 95% CL constraints for *Planck* data comparing the canonical Lagrangian case with $c_s = 1$ to the case of varying c_s with a uniform prior $0.024 < c_s < 1$ derived from the *Planck* NG measurements.

(Garriga & Mukhanov 1999; Chen et al. 2007). Section 10.2 focuses on a specific example of a single-field model of inflation with more general higher-derivative operators, the so-called "Galileon inflation". Section 10.3 presents constraints on axion monodromy inflation. See Planck Collaboration XVII (2016) for the analysis of other interesting non-standard inflationary models, including warm inflation (Berera 1995), whose $f_{\rm NL}$ predictions can be constrained by *Planck*.

10.1. Inflation with a non-standard kinetic term

This class of models includes k-inflation (Armendáriz-Picón 1999; Garriga & Mukhanov 1999) and Dirac-Born-Infield (DBI) models introduced in the context of brane inflation (Silverstein & Tong 2004; Alishahiha et al. 2004; Chen 2005b,a). In these models inflation can take place despite a steep potential or may be driven by the kinetic term.

Moreover, one of the main predictions of inflationary models with a non-standard kinetic term is that the inflaton perturbations can propagate with a sound speed $c_{\rm s} < 1$. We show how the *Planck* combined measurement of the power spectrum and the nonlinearity parameter $f_{\rm NL}$ (Planck Collaboration XVII 2016) improves constraints on this class of models by breaking degeneracies between the parameters determining the observable power spectra. Such degeneracies (see, e.g., Peiris et al. 2007; Powell et al. 2009; Lorenz et al. 2008; Agarwal & Bean 2009; Baumann et al. 2015) are evident from the expressions for the power spectra. We adopt the same notation as Planck Collaboration XXIV (2014). At leading order in the slow-roll parameters the scalar power spectrum depends additionally on the sound speed $c_{\rm s}$ via (Garriga & Mukhanov 1999)

$$A_{\rm s} \approx \frac{1}{8\pi^2 M_{\rm pl}^2}\frac{H^2}{c_{\rm s}\epsilon_1}, \tag{86}$$

which is evaluated at $kc_{\rm s} = aH$. Correspondingly, the scalar spectral index

$$n_{\rm s} - 1 = -2\epsilon_1 - \epsilon_2 - s \tag{87}$$

depends on an additional slow-roll parameter $s = \dot{c}_{\rm s}/(c_{\rm s}H)$, which describes the running of the sound speed. The usual consistency relation holding for the standard single-field models of slow-roll inflation ($r = -8n_{\rm t}$) is modified to $r \approx -8n_{\rm t}c_{\rm s}$, with $n_{\rm t} = -2\epsilon_1$ as usual (Garriga & Mukhanov 1999), potentially allowing models which otherwise would predict a large tensor-to-scalar ratio for the Klein-Gordon case (Unnikrishnan et al. 2012).[10]

At lowest order in the slow-roll parameters, there are strong degeneracies between the parameters $(A_{\rm s}, c_{\rm s}, \epsilon_1, \epsilon_2, s)$. This makes the constraints on these parameters from the power spectrum alone not very stringent, and for parameters like ϵ_1 and ϵ_2 less stringent compared with the standard case. However, combining the constraints on the power spectra observables with those on $f_{\rm NL}$ can also result in a stringent test for this class of inflationary models. Models where the inflaton field has a non-standard kinetic term predict a high level of primordial NG of the scalar perturbations for $c_{\rm s} \ll 1$, (see, e.g., Chen et al. 2007). Primordial NG is generated by the higher-derivative interaction terms arising from the expansion of the kinetic part of the Lagrangian, $P(\phi, X)$. There are two main contributions to the amplitude of the NG (i.e., to the nonlinearity parameter $f_{\rm NL}$), coming from the inflaton field interaction terms $\dot{\delta\phi}\,(\nabla\delta\phi)^2$ and $(\dot{\delta\phi})^3$ (Chen et al. 2007; Senatore et al. 2010). The NG from the first term scales as $c_{\rm s}^{-2}$, while the NG arising from the other term is determined by a second parameter, $\tilde{c}_3$ (following the notation of Senatore et al. 2010). Each of these two interactions produces bispectrum shapes similar to the so-called *equilateral* shape (Babich et al. 2004) for which the signal peaks for equilateral triangles with $k_1 = k_2 = k_3$. (These two shapes are called, respectively, "EFT1" and "EFT2" in Planck Collaboration XVII 2016). However, the difference between the two shapes is such that the total signal is a linear combination of the two, leading to an "orthogonal" bispectral template (Senatore et al. 2010).

The equilateral and orthogonal NG amplitudes can be expressed in terms of the two "microscopic" parameters, $c_{\rm s}$ and $\tilde{c}_3$

[10] We use the more accurate relation

$$r = 16\epsilon_1 c_{\rm s}^{(1+\epsilon_1)/(1-\epsilon_1)}, \tag{88}$$

accounting for different epochs of freeze-out for the scalar fluctuations (at sound horizon crossing, $kc_{\rm s} = aH$) and tensor perturbations (at Hubble radius crossing, $k = aH$; Peiris et al. 2007; Powell et al. 2009; Lorenz et al. 2008; Agarwal & Bean 2009; Baumann et al. 2015).

(for more details see Planck Collaboration XVII 2016), according to

$$f_{\rm NL}^{\rm equil} = \frac{1-c_{\rm s}^2}{c_{\rm s}^2}\left[-0.275 - 0.0780 c_s^2 - (2/3)\times 0.780\,\tilde{c}_3\right], \quad (89)$$

$$f_{\rm NL}^{\rm ortho} = \frac{1-c_{\rm s}^2}{c_{\rm s}^2}\left[0.0159 - 0.0167 c_s^2 - (2/3)\times 0.0167\,\tilde{c}_3\right]. \quad (90)$$

Thus the measurements of $f_{\rm NL}^{\rm equil}$ and $f_{\rm NL}^{\rm ortho}$ obtained in the companion paper (Planck Collaboration XVII 2016) provide a constraint on the sound speed, $c_{\rm s}$, of the inflaton field. Such constraints allow us to combine the NG information with the analyses of the power spectra, since the sound speed is the NG parameter also affecting the power spectra.

In this subsection we consider three cases. In the first case we perform a general analysis as described above (focusing on the simplest case of a constant sound speed, $s = 0$), improving on PCI13 and Planck Collaboration XXIV (2014) by exploiting the full mission temperature and polarization data. The *Planck* constraints on primordial NG in general single-field models of inflation provide the most stringent bound on the inflaton sound speed (Planck Collaboration XVII 2016):[11]

$$c_{\rm s} \geq 0.024 \quad (95\%\ {\rm CL}). \quad (91)$$

We then use this information on $c_{\rm s}$ as a uniform prior $0.024 \leq c_{\rm s} \leq 1$ in Eq. (88) within the HFF formalism, as in PCI13. Figure 35 shows the joint constraints on ϵ_1 and ϵ_2. *Planck* TT+lowP yields $\epsilon_1 < 0.031$ at 95% CL. No improvement in the upper bound on ϵ_1 results when using *Planck* TT, TE, EE+lowP. This constraint improves the previous analysis in PCI13 and can be compared with the restricted case of $c_{\rm s} = 1$, also shown in Fig. 35, with $\epsilon_1 < 0.0068$ at 95% CL. The limits on the sound speed from the constraints on primordial NG are crucial for deriving an upper limit on ϵ_1, because the relation between the tensor-to-scalar ratio and ϵ_1 also involves the sound speed (see, e.g., Eq. (88)). This breaks the degeneracy in the scalar spectral index.

The other two cases analysed involve DBI models. The degeneracy between the different slow-roll parameters can be broken for $s = 0$ or in the case where $s \propto \epsilon_2$. We first consider models defined by an action of the DBI form

$$P(\phi, X) = -f(\phi)^{-1}\sqrt{1 - 2f(\phi)X} + f(\phi)^{-1} - V(\phi), \quad (92)$$

where $V(\phi)$ is the potential and $f(\phi)$ describes the warp factor determined by the geometry of the extra dimensions. We follow an analogous procedure to exploit the NG limits derived in Planck Collaboration XVII (2016) on $c_{\rm s}$ in the case of DBI models: $c_{\rm s} \geq 0.087$ (at 95% CL). Assuming a uniform prior, $0.087 \leq c_{\rm s} \leq 1$, and $s = 0$, *Planck* TT+lowP gives $\epsilon_1 < 0.024$ at 95% CL, a 43% improvement with respect to PCI13. The addition of high-ℓ TE and EE does not improve the upper bound on ϵ_1 for this DBI case.

Next we update the constraints on the particularly interesting case of infrared DBI models (Chen 2005b,a), where $f(\phi) \approx \lambda/\phi^4$. (For details, see Silverstein & Tong 2004; Alishahiha et al. 2004; Chen et al. 2007, and references therein.) In these models the inflaton field moves from the IR to the UV side with an inflaton potential

$$V(\phi) = V_0 - \frac{1}{2}\beta H^2\phi^2. \quad (93)$$

From a theoretical point of view a wide range of values for β is allowed: $0.1 < \beta < 10^9$ (Bean et al. 2008). PCI13 dramatically restricted the allowed parameter space of these models in the limit where stringy effects can be neglected and the usual field theory computation of the primordial curvature perturbation holds (see Chen 2005a,c; Bean et al. 2008 for more details). In this limit of the IR DBI model, one finds (Chen 2005c; Chen et al. 2007) $c_{\rm s} \approx (\beta N_*/3)^{-1}$, $n_{\rm s} - 1 = -4/N_*$, and ${\rm d}n_{\rm s}/{\rm d}\ln k = -4/N_*^2$. (In this model one can verify that $s \approx 1/N_* \approx \epsilon_2/3$.) Combining the uniform prior on $c_{\rm s}$ with *Planck* TT+lowP, we obtain

$$\beta \leq 0.31 \quad (95\%\ {\rm CL}), \quad (94)$$

and a preference for a high number of e-folds: $78 < N_* < 157$ at 95% CL.

We now constrain the general case of the IR DBI model, including the "stringy" regime, which occurs when the inflaton extends back in time towards the IR side (Bean et al. 2008). The stringy phase transition is characterized by an interesting phenomenology altering the predictions for cosmological perturbations. A parameterization of the power spectrum of curvature perturbations interpolating between the two regimes is (Bean et al. 2008; see also Ma et al. 2013)

$$\mathcal{P}_{\mathcal{R}}(k) = \frac{A_{\rm s}}{\left(N_{\rm e}^{\rm DBI}\right)^4}\left[1 - \frac{1}{(1+x)^2}\right], \quad (95)$$

where $A_{\rm s} = 324\pi^2/(n_{\rm B}\beta^4)$ is the amplitude of the perturbations which depends on various microscopic parameters ($n_{\rm B}$ is the number of branes at the B-throat; see Bean et al. 2008 for more details), while $x = (N_{\rm e}^{\rm DBI}/N_{\rm c})^8$ sets the stringy phase transition taking place at the critical e-fold $N_{\rm c}$. (Here $N_{\rm e}^{\rm DBI}$ is the number of e-folds to the end of IR DBI inflation.) The spectral index and its running are

$$n_{\rm s} - 1 = \frac{4}{N_{\rm e}^{\rm DBI}}\frac{x^2 + 3x - 2}{(x+1)(x+2)}, \quad (96)$$

$$\frac{{\rm d}n_{\rm s}}{{\rm d}\ln k} = \frac{4}{\left(N_{\rm e}^{\rm DBI}\right)^2}\frac{x^4 + 6x^3 - 55x^2 - 96x - 4}{(x+1)^2(x+2)^2}. \quad (97)$$

A prediction for the primordial NG in the stringy regime is not available. We assume the standard field-theoretic result for a primordial bispectrum of the equilateral type with an amplitude $f_{\rm NL}^{\rm DBI} = -(35/108)\,[(\beta^2\,(N_{\rm e}^{\rm DBI})^2/9) - 1]$. By considering the same uniform prior on $c_{\rm s}$, we obtain $\beta < 0.77$, $66 < N_{\rm e}^{\rm DBI} < 72$, and $x < 0.41$ at 95% CL, which severely limits the general IR DBI model and strongly restricts the allowed parameter space.

10.2. Galileon inflation

As a further example of the implications of the NG constraints on (non-standard) inflationary models we consider Galileon inflation Burrage et al. (2011; see also Kobayashi et al. 2010; Mizuno & Koyama 2010; Ohashi & Tsujikawa 2012). This represents a well-defined and well-motivated model of inflation with more general higher derivatives of the inflaton field compared to the

[11] This section uses results based on $f_{\rm NL}$ constraints from T and E (Planck Collaboration XVII 2016). In Planck Collaboration XVII (2016) it is shown that, although conservatively considered as preliminary, the $f_{\rm NL}$ constraints from T and E are robust, since they pass an extensive battery of validation tests and are in full agreement with T-only constraints.

non-standard kinetic term case analysed above. The Galileon models of inflation are based on the so-called "Galilean symmetry" (Nicolis et al. 2009), and enjoy some well understood stability properties (absence of ghost instabilities and protection from large quantum corrections). This makes the theory also very predictive, since observable quantities (scalar and tensor power spectra and higher-order correlators) depend on a finite number of parameters. From this point of view this class of models shares some of the same properties as the DBI inflationary models (Silverstein & Tong 2004; Alishahiha et al. 2004). The Galileon field arises naturally within fundamental physics constructions (e.g., de Rham & Gabadadze 2010b,a). These models also offer an interesting example of large-scale modifications to Einstein gravity.

The Galileon model is based on the action (Deffayet et al. 2009a,b)

$$S = \int \mathrm{d}^4x\,\sqrt{-g}\left(\frac{M_{\rm pl}^2}{2}R + \sum_{n=0}^{3}\mathcal{L}_n\right), \tag{98}$$

where

$$\mathcal{L}_0 = c_2 X, \tag{99}$$

$$\mathcal{L}_1 = -2\left(c_3/\Lambda^3\right)X\Box\phi, \tag{100}$$

$$\mathcal{L}_2 = 2\left(c_4/\Lambda^6\right)X\left[(\Box\phi)^2 - \left(\nabla_\mu\nabla_\nu\phi\right)^2\right] + \left(c_4/\Lambda^6\right)X^2R, \tag{101}$$

$$\mathcal{L}_3 = -2\left(c_5/\Lambda^9\right)X\left[(\Box\phi)^3 - 3\Box\phi\left(\nabla_\mu\nabla_\nu\phi\right)^2 + 2\left(\nabla_\mu\nabla_\nu\phi\right)^3\right] + 6\left(c_5/\Lambda^9\right)X^2G_{\mu\nu}\nabla^\mu\nabla^\nu\phi. \tag{102}$$

Here $X = -\nabla_\mu\phi\nabla^\mu\phi/2$, $(\nabla_\mu\nabla_\nu\phi)^2 = \nabla_\mu\nabla_\nu\phi\nabla^\mu\nabla^\nu\phi$, and $(\nabla_\mu\nabla_\nu\phi)^3 = \nabla_\mu\nabla_\nu\phi\nabla^\mu\nabla^\rho\phi\nabla^\nu\nabla_\rho\phi$. The coupling coefficients c_i are dimensionless and Λ is the cutoff of the theory. The case of interest includes a potential term $V(\phi) = V_0 + \lambda\phi + (1/2)m^2\phi^2 + \ldots$ to drive inflation.

The predicted scalar power spectrum at leading order is (Ohashi & Tsujikawa 2012; Burrage et al. 2011; Tsujikawa et al. 2013; see also Kobayashi et al. 2011a; Gao & Steer 2011)[12]

$$\mathcal{P}_\mathcal{R} = \left.\frac{H^2}{8\pi^2M_{\rm Pl}^2\epsilon_{\rm s}Fc_{\rm s}}\right|_{c_{\rm s}k=aH} = \frac{H^4}{8\pi^2A(\dot\phi_0)^2c_{\rm s}^3}, \tag{104}$$

where $F = 1 + \bar{c}_4(\dot\phi_0)^2/(2H^2M_{\rm Pl}^2)$ and $c_{\rm s}^2 = -B/A$ is the sound speed of the Galileon field. $\epsilon_{\rm s}$ is different from the usual slow-roll parameter ϵ_1 and at leading order related according to $\epsilon_{\rm s} = -2B/(1 + 6\bar{c}_3 + 18\bar{c}_4 + 30\bar{c}_5)\epsilon_1$. The scalar spectral index

$$n_{\rm s} - 1 = -2\epsilon_1 - \eta_{\rm s} - s \tag{105}$$

depends on the slow-roll parameters ϵ_1, $\eta_{\rm s} = \dot\epsilon_{\rm s}/(H\epsilon_{\rm s})$, and $s = \dot c_{\rm s}/(Hc_{\rm s})$. As usual the slow-roll parameter s describes the running of the sound speed. In the following we restrict ourselves to the case of a constant sound speed with $s = 0$. The tensor-to-scalar ratio is

$$r = 16\epsilon_s c_{\rm s} = 16\epsilon_1\bar{c}_{\rm s}, \tag{106}$$

where we have introduced the parameter $\bar{c}_{\rm s} = -[2B/(1 + 6\bar{c}_3 + 18\bar{c}_4 + 30\bar{c}_5)]c_{\rm s}$, which is related to the Galileon sound speed. The parameter $\bar{c}_{\rm s}$ can be either positive or negative. In the negative branch a blue spectral tilt for the primordial gravitational waves is allowed, contrary to the situation for standard slow-roll models of inflation. We introduce such a quantity so that the consistency relation takes the form $r \approx -8n_{\rm t}\bar{c}_{\rm s}$, with $n_{\rm t} = -2\epsilon_1$, analogous to Eq. (88). The measurements of primordial NG constrain $\bar{c}_{\rm s}$, which in turn constrains ϵ_1 and $\eta_{\rm s}$ in Eq. (105). This is analogous to the constraints on ϵ_1 and η of Eq. (87) in the previous subsection.

Galileon models of inflation predict interesting NG signatures (Burrage et al. 2011; Tsujikawa et al. 2013).[13] We have verified (see also Creminelli et al. 2011) that bispectra can be generated with the same shapes as the "EFT1" and "EFT2" (Senatore et al. 2010; Chen et al. 2007) constrained in the companion paper (Planck Collaboration XVII 2016), which usually arise in models of inflation with non-standard kinetic terms, with

$$f_{\rm NL}^{\rm EFT1} = \frac{17}{972}\left(-\frac{5}{c_{\rm s}^4} + \frac{30}{c_{\rm s}^2} - \frac{40}{c_{\rm s}\bar{c}_{\rm s}} + 15\right), \tag{107}$$

$$f_{\rm NL}^{\rm EFT2} = \frac{1}{243}\left(\frac{5}{c_{\rm s}^4} + \frac{30/A - 55}{c_{\rm s}^2} + \frac{40}{c_{\rm s}\bar{c}_{\rm s}} - 320\frac{c_{\rm s}}{\bar{c}_{\rm s}} - \frac{30}{A} + 275 - 225c_{\rm s}^2 + 280\frac{c_{\rm s}^3}{\bar{c}_{\rm s}}\right). \tag{108}$$

As explained in the previous subsection, the linear combinations of these two bispectra produce both equilateral and orthogonal bispectrum templates. Given Eqs. (104)–(108), we can proceed as in the previous section to exploit the limits on primordial NG in a combined analysis with the power spectra analysis. In Planck Collaboration XVII (2016) the constraint $c_{\rm s} \geq 0.23$ (95% CL) is obtained based on the constraints on $f_{\rm NL}^{\rm equil}$ and $f_{\rm NL}^{\rm ortho}$. One can proceed as described in Planck Collaboration XVII (2016) to constrain the parameter $\bar{c}_{\rm s}$ modifying the consistency relation, Eq. (106). Adopting a log-uniform prior on A in the interval $10^{-4} \leq A \leq 10^4$ and a uniform prior $10^{-4} \leq c_{\rm s} \leq 1$, the *Planck* measurements on $f_{\rm NL}^{\rm equil}$ and $f_{\rm NL}^{\rm ortho}$ constrain $\bar{c}_{\rm s}$ to be $0.038 \leq \bar{c}_{\rm s} \leq 100$ (95% CL) (Planck Collaboration XVII 2016). We also explore the possibility of the negative branch (corresponding to a blue tensor spectral index), finding $-100 \leq \bar{c}_{\rm s} \leq -0.034$ (95% CL) (Planck Collaboration XVII 2016). By allowing a logarithmic prior on $\bar{c}_{\rm s}$ based on the $f_{\rm NL}$ measurements, Fig. 36 shows the joint constraints on ϵ_1 and $\eta_{\rm s}$ for the $n_{\rm t} < 0$ branch and for the $n_{\rm t} > 0$ branch. *Planck* TT+lowP+BAO and the NG bounds on $\bar{c}_{\rm s}$ constrain $\epsilon_1 < 0.036$ at 95% CL for $n_{\rm t} < 0$ (and $|\epsilon_1| < 0.041$ for $n_{\rm t} > 0$).

10.3. Axion monodromy inflation

10.3.1. Introduction

The mechanism of monodromy inflation (Silverstein & Westphal 2008; McAllister et al. 2010; Kaloper et al. 2011; Flauger et al. 2014b) in string theory motivates a broad class of inflationary potentials of the form

$$V(\phi) = \mu^{4-p}\phi^p + \Lambda_0^4\,\mathrm{e}^{-C_0\left(\frac{\phi}{\phi_0}\right)^{p_\Lambda}}\cos\left[\gamma_0 + \frac{\phi_0}{f_0}\left(\frac{\phi}{\phi_0}\right)^{p_f+1}\right]. \tag{109}$$

[12] For the following expressions it is convenient to define the quantities

$$A = c_2/2 + 6\bar{c}_3 + 27\bar{c}_4 + 60\bar{c}_5, \quad B = -c_2/2 - 4\bar{c}_3 - 13\bar{c}_4 - 24\bar{c}_5, \tag{103}$$

where $\bar{c}_i = c_iZ^{i-2}$ for $i = 2$ to 5, with $Z = H\dot\phi_0/\Lambda^3$. In order to have a viable model we require $A > 0$ (no ghosts) and $B < 0$ (no gradient instabilities).

[13] See also Mizuno & Koyama (2010), Gao & Steer (2011), Kobayashi et al. (2011b), De Felice & Tsujikawa (2013), and Regan et al. (2015).

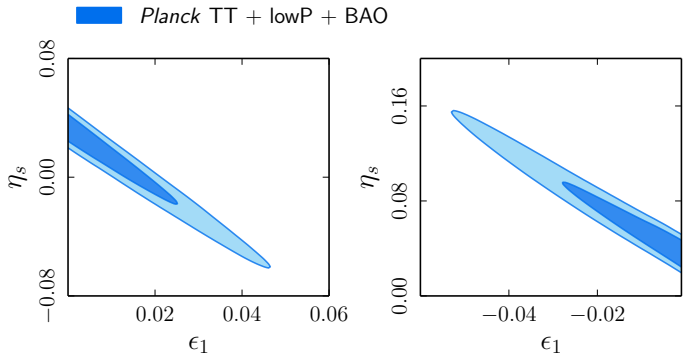

Fig. 36. Marginalized joint 68% and 95% CL for the Galileon parameters (ϵ_1, η_s) for $n_t < 0$ (*left panel*) and $n_t > 0$ (*right panel*).

Here μ, Λ_0, f_0, and ϕ_0 are constants with the dimension of mass and C_0, p, p_Λ, p_f, and γ_0 are dimensionless.

In simpler parameterizations used in prior analyses of oscillations from axion monodromy inflation (Peiris et al. 2013; Planck Collaboration XXII 2014; Easther & Flauger 2014; Jackson et al. 2014; Meerburg et al. 2014b,a; Meerburg & Spergel 2014; Meerburg 2014), one assumes $p_\Lambda = p_f = 0$, corresponding to a sinusoidal term with constant amplitude throughout inflation taken to be a periodic function of the canonically-normalized inflaton ϕ. Taking $p_\Lambda \neq 0$ and $p_f \neq 0$ allows the *magnitude* and *frequency*, respectively, of the modulation to depend on ϕ. For example, the frequency is always a periodic function of an underlying angular axion field, but its relation to the canonically normalized inflaton field is model-dependent.

The microphysical motivation for $p_\Lambda \neq 0$ and $p_f \neq 0$ is that in string theory additional scalar fields, known as "moduli," evolve during inflation. The inflationary potential depends on a subset of these fields. Because the magnitude and frequency of modulations are determined by the vacuum expectation values of moduli, both quantities are then naturally functions of ϕ. The case $p_\Lambda = p_f = 0$ corresponds to when these fields are approximately fixed, stabilized strongly by additional terms in the scalar potential. But in other cases, the axion potential that drives inflation also provides a leading term stabilizing the moduli. The exponential dependence of the magnitude in the potential of Eq. (109) arises because the modulations are generated non-perturbatively, e.g., by instantons. For this reason, the modulations can be undetectably small in this framework, although there are interesting regimes where they could be visible.

Specific examples studied thus far yield exponents p, p_Λ, and p_f that are rational numbers of modest size. For example, models with $p = 3, 2, 4/3, 1$, and $2/3$ have been constructed (Silverstein & Westphal 2008; McAllister et al. 2010, 2014), or in another case $p = 4/3$, $p_\Lambda = -1/3$, and $p_f = -1/3$. Following Flauger et al. (2014b), we investigate the effect of a drift in frequency arising from p_f, neglecting a possible drift in the modulation amplitude by setting $p_\Lambda = C_0 = 0$. Even in this restricted model, a parameter exploration using a fully numerical computation of the primordial power spectrum following the methodology of Peiris et al. (2013) is prohibitive, so we follow Flauger et al. (2014b) to study two templates capturing the features of the primordial spectra generated by this potential.

The first template, which we call the "semi-analytic" template, is given by

$$\mathcal{P}_\mathcal{R}(k) = \mathcal{P}_\mathcal{R}(k_*)\left(\frac{k}{k_*}\right)^{n_s-1}\left\{1 + \delta n_s \cos\left[\frac{\phi_0}{f}\left(\frac{\phi_k}{\phi_0}\right)^{p_f+1} + \Delta\phi\right]\right\}. \tag{110}$$

The parameter f is higher than the underlying axion decay constant f_0 of the potential by a few percent, but this difference will be neglected in this analysis. The quantity ϕ_0 is some fiducial value for the scalar field, and ϕ_k is the value of the scalar field at the time when the mode with comoving momentum k exits the Hubble radius. At leading order in the slow-roll expansion, in units where the reduced Planck mass $M_{\rm Pl} = 1$, $\phi_k = \sqrt{2p\,(N_0 - \ln(k/k_*))}$, where $N_0 = N_* + \phi_{\rm end}^2/(2p)$, and $\phi_{\rm end}$ is the value of the scalar field at the end of inflation.

The second "analytic" template was derived by Flauger et al. (2014b) by expanding the argument of the trigonometric function in Eq. (110) in $\ln(k/k_*)$, leading to

$$\mathcal{P}_\mathcal{R}(k) = \mathcal{P}_\mathcal{R}(k_*)\left(\frac{k}{k_*}\right)^{n_s-1} \times\left\{1 + \delta n_s \cos\left[\Delta\phi + \alpha\left(\ln\left(\frac{k}{k_*}\right) + \sum_{n=1}^{2}\frac{c_n}{N_*^n}\ln^{n+1}\left(\frac{k}{k_*}\right)\right)\right]\right\}. \tag{111}$$

The relation between the empirical parameters in the templates and the potential parameters are approximated by $\delta n_s = 3b\sqrt{2\pi/\alpha}$, where

$$\alpha = (1 + p_f)\frac{\phi_0}{2fN_0}\left(\frac{\sqrt{2pN_0}}{\phi_0}\right)^{1+p_f}, \tag{112}$$

and b is the monotonicity parameter defined in Flauger et al. (2014b), providing relations converting bounds on c_n into bounds on the microphysical parameters of the potential. However, the analytic template can describe more general shapes of primordial spectra than just axion monodromy.

As discussed by Flauger et al. (2014b), there is a degeneracy between p (or alternatively n_s) and f. For both templates we fix $p = 4/3$ and also fix the tensor power spectrum to its form in the absence of oscillations. This is an excellent approximation because tensor oscillations are suppressed relative to the scalar oscillations by a factor $\alpha(f/M_{\rm Pl})^2 \ll 1$. A uniform prior $-\pi < \Delta\phi < \pi$ is adopted for the phase parameter of both templates as well as a prior $0 < \delta n_s < 0.7$ for the modulation amplitude parameter.

In order to specify the semi-analytic template, we assume instantaneous reheating, which for $p = 4/3$ corresponds to $N_* \approx 57.5$ for $k_* = 0.05\,{\rm Mpc}^{-1}$. We set $\phi_0 = 12.38 M_{\rm Pl}$ with $\phi_{\rm end} = 0.59 M_{\rm Pl}$. We adopt uniform priors $-4 < \log_{10}(f/M_{\rm Pl}) < -1$ and $-0.75 < p_f < 1$ for the remaining parameters. The priors $0 < \ln(\alpha) < 6.9$ and $-2 < c_{1,2} < 2$ specify the *analytic* template. The single-field effective field theory becomes strongly coupled for $\alpha > 200$. However, in principle the string construction remains valid in this regime.

10.3.2. Power spectrum constraints on monodromy inflation

We carry out a Bayesian analysis of axion monodromy inflation using a high-resolution version of `CAMB` coupled to the `PolyChord` sampler (see Sect. 8.2). For our baseline analysis we conservatively adopt *Planck* TT+lowP, using the "bin1" high-ℓ *TT* likelihood. In addition to the primordial template priors specified above, we marginalize over the standard priors for the cosmological parameters, the primordial amplitude, and foreground parameters.

The marginalized joint posterior constraints on pairs of primordial parameters for the analytic and semi-analytic templates are shown in Figs. 37 and 38, respectively.

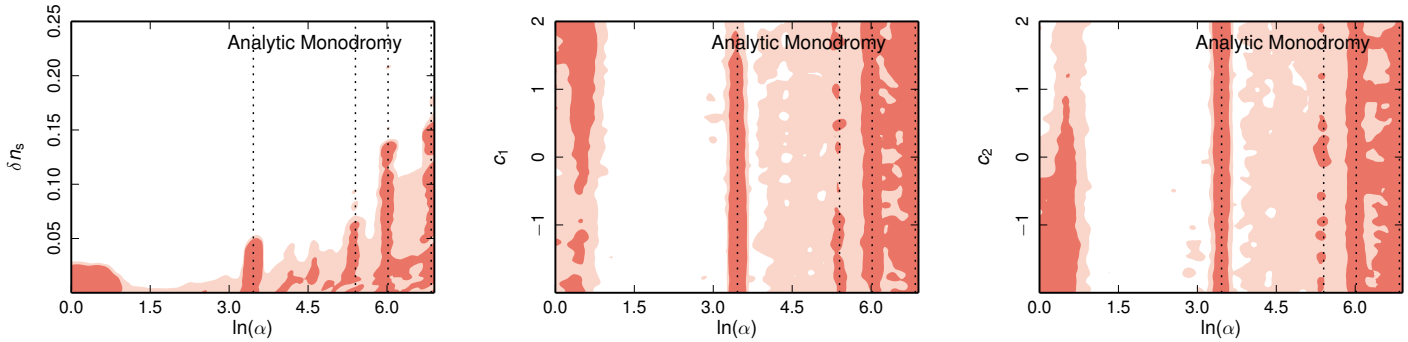

Fig. 37. Constraints on the parameters of the analytic template, showing joint 68% and 95% CL. The dotted lines correspond to the frequencies showing the highest-likelihood improvements (see text).

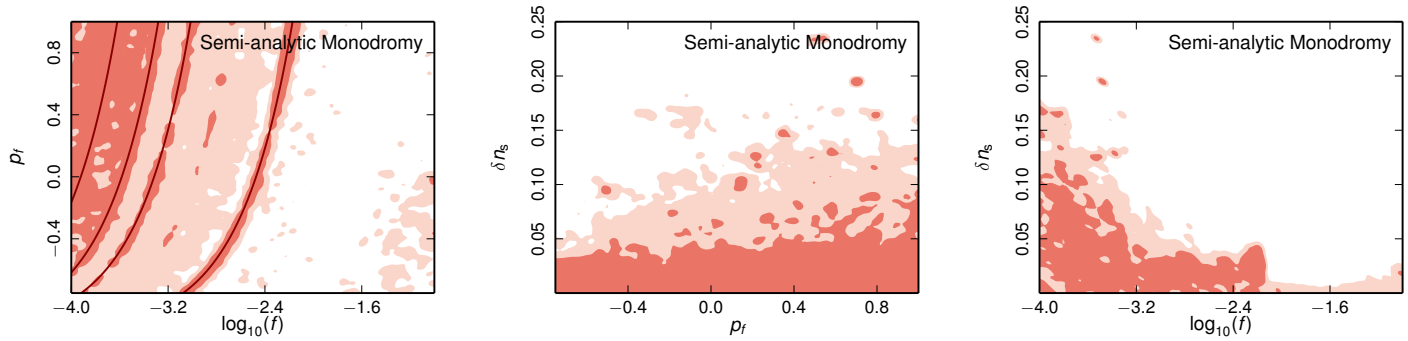

Fig. 38. Constraints on the parameters of the semi-analytic template showing joint 68% and 95% CL. The solid lines on the left-hand panel mark the frequencies showing the highest-likelihood improvements (see text).

The complex structures seen in these plots arise due to degeneracies in the likelihood frequency "beating" between underlying modulations in the data and the model (Easther et al. 2005). Parameter combinations where "beating" occurs over the largest k ranges lead to discrete local maxima in the likelihood. Fortuitous correlations in the observed realization of the C_ℓ can give the same effect.

The four frequencies picked out by these structures, $\ln(\alpha) \approx \{3.5, 5.4, 6.0, 6.8\}$, show improvements of $\Delta\chi^2 \approx \{-9.7, -7.1, -12.2, -12.5\}$ relative to ΛCDM, respectively. These frequencies are marked by dotted lines in Fig. 37, and by solid lines in Fig. 38 using Eq. (112). The semi-analytic and analytic templates lead to self-consistent results as expected, with analogous structures being picked out by the likelihood in each template. There is no evidence for a drifting frequency, $p_f \neq 0$ or $c_n \neq 0$. Thus, these parameters serve to smooth out structures in the marginalized posterior.

The improvement in χ^2 is not compelling enough to suggest a primordial origin. Fitting a modulated model to simulations with a smooth spectrum can give rise to $\Delta\chi^2 \sim -10$ improvements (Flauger et al. 2014b). Furthermore, as the monodromy model contains only a single frequency, at least three of these structures must correspond to spurious fits to the noise. Considering the two models defined by the two templates and the parameter priors specified above, the Bayes factors calculated using `PolyChord` favours base ΛCDM over both templates by odds of roughly 8:1.

Compared to previous analyses of the linear ($p = 1$) axion monodromy model for WMAP9 (Peiris et al. 2013) and the 2013 *Planck* data (Planck Collaboration XXII 2014; Easther & Flauger 2014) the common frequencies are shifted slightly upward. The lower frequency in common appears shifted by a factor of order $\sqrt{p}$ from $\alpha \approx 28.9$ to 31.8 and the higher frequency in common from $\alpha \approx 210$ to 223. Flauger et al. (2014b) suggest that the lower frequency (which had $\Delta\chi^2 = -9$ in PCI13) was associated with the 4 K cooler line systematic effects in the 2013 *Planck* likelihood. However, its presence at similar significance in the 2015 likelihood with improved handling of the cooler line systematics suggests that this explanation is not correct. The second frequency, which appeared with $\Delta\chi^2 \approx -20$ in WMAP9 (Peiris et al. 2013) is still present but with much reduced significance, suggesting that the high multipoles do not give evidence for this frequency. Additionally, two higher frequencies are present, which if interpreted as being of primordial origin, correspond to a regime well beyond the validity of the single-field effective field theory. If one of these frequencies were to be confirmed as primordial, a significantly improved understanding of the underlying string construction would need to be undertaken.

In order to check whether the improvement in fit at these four modulation frequencies is responding to residual foregrounds or other systematics, we examine the frequency residuals. Figure 39 shows the residuals of the data minus the model (including the best-fit foreground model) for the four `PLIK` frequency combinations binned at $\Delta\ell = 30$ for the lowest modulation frequency, $\ln(\alpha) \approx 3.5$. This plot shows no significant frequency dependence, and thus there is no indication that the fit is responding to frequency dependent systematics. Furthermore, the plot does not show evidence that the improvement for this modulation frequency comes from the feature at $\ell \approx 800$, as suggested by Easther & Flauger (2014). This feature and another at $\ell \approx 1500$ are apparent at all frequency combinations. Similar plots for the

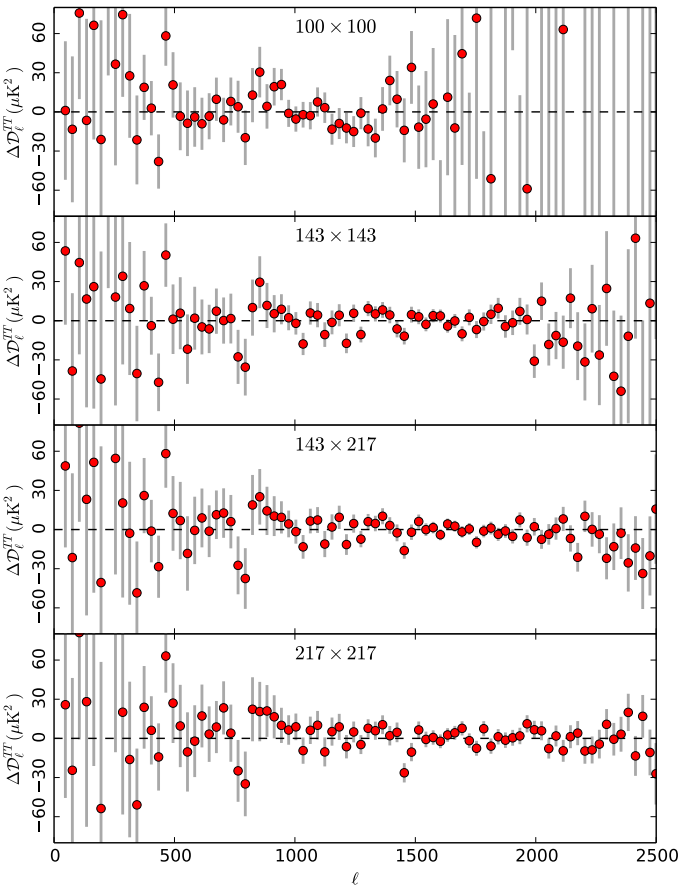

Fig. 39. Frequency residuals for the $\ln(\alpha) \approx 3.5$ likelihood peak, binned at $\Delta\ell = 30$. The $\pm1\sigma$ errors are given by the square root of the diagonal elements of the covariance matrix.

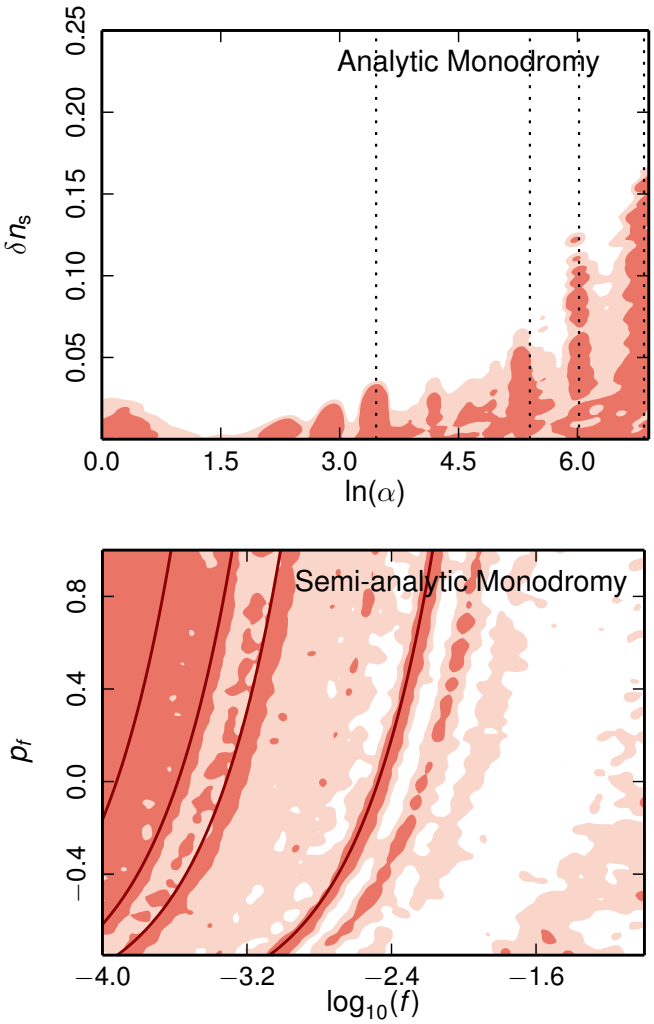

Fig. 40. Constraints on the parameters of the analytic (*top*) and semi-analytic (*bottom*) templates with the addition of high-ℓ polarization data in the likelihood, showing joint 68% and 95% CL. The lines mark the frequencies showing the highest-likelihood improvements identified in the baseline temperature-only analysis.

three other modulation frequencies also do not show indications of frequency dependence.

In order to confirm whether any of the frequencies picked out here is of primordial origin, one can exploit independent information in the polarization data to perform a cross-check of the temperature prediction, thus minimizing the "look-elsewhere" effect (Mortonson et al. 2009). Leaving a complete analysis of the independent information in the polarization for future work, we now check whether the temperature-only result remains stable when high-ℓ polarization is added in the likelihood. In Fig. 40 we show a preliminary analysis using the PLIK temperature and polarization (*TT*, *TE*, and *EE*) "bin1" likelihood plus low-ℓ polarization data. A comparison with the left-hand panels of Figs. 37 and 38 indicates slight differences from the T-only analysis. However, all the four frequencies identified in the temperature are present when high-ℓ polarization is added. There is a maximum $\Delta\chi^2 \approx -8.0$ improvement over ΛCDM. We also repeat the analysis using only the *EE* polarization "bin1" likelihood plus low-ℓ temperature and polarization data. These results are presented in Fig. 41. The *EE*-only frequencies are offset with respect to the temperature-only frequencies: the best-fit *EE*-only frequencies are at $\ln(\alpha) \approx \{3.8, 5.0, 5.4, 5.8, 6.2\}$. The maximum improvement over ΛCDM for this case is $\Delta\chi^2 \approx -12.5$.

10.3.3. Predictions for resonant non-Gaussianity

The left-hand panel of Fig. 42 presents derived constraints on the parameters of the potential in Eq. (109) calculated using the analytic template. Another cross-check of primordial origin is available since the monodromy model predicts resonant NG, generating a bispectrum whose properties would be strongly correlated with that of the power spectrum (Chen et al. 2008; Flauger & Pajer 2011). Using the mapping

$$f_{\rm NL}^{\rm res} = \frac{\delta n_{\rm s}}{8}\alpha^2, \tag{113}$$

we use the analytic template to derive the posterior probability for the resonant NG signal predicted by constraints from the power spectrum, presented in the middle and right panels of Fig. 42.

Planck Collaboration XVII (2016) use an improved modal estimator to scan for resonant NG. The resolution of this scan is currently limited to $\ln(\alpha) < 3.9$, which potentially can probe the lowest frequency picked out in the power spectrum search. However, the modal estimator's sensitivity (imposed by cosmic variance) of $\Delta f_{\rm NL}^{\rm res} \approx 80$ is significantly greater than the predicted value for this frequency from fits to the power spectrum,

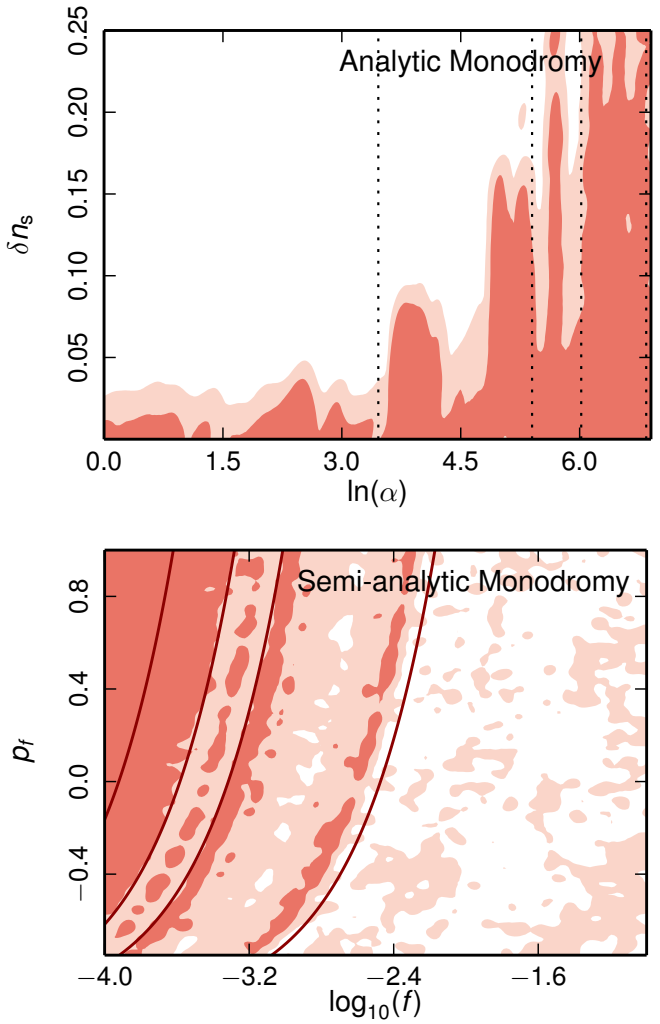

Fig. 41. Constraints on the parameters of the analytic (*top*) and semi-analytic (*bottom*) templates with *EE*-only high-ℓ polarization data plus low-ℓ temperature and polarization data, showing joint 68% and 95% CL. The lines mark the frequencies showing the highest-likelihood improvements identified in the baseline temperature-only analysis.

$f_{\rm NL}^{\rm res} \sim 10$. Efforts to increase the resolution of the modal estimator are ongoing and may allow consistency tests of the significantly higher levels of resonant NG predicted by the higher frequencies in the future.

10.3.4. Power spectrum and bispectrum constraints on axion inflation with a gauge field coupling

We now consider the case where the axion field is coupled to a gauge field. Such a scenario is physically well motivated. From an effective field theory point of view the derivative coupling is natural and must be included since it respects the same shift symmetry that leads to axion models of inflation (Anber & Sorbo 2010; Barnaby & Peloso 2011; Pajer & Peloso 2013). This type of coupling is also ubiquitous in string theory (see, e.g., Barnaby et al. 2012; Linde et al. 2013). The coupling term in the action is (Anber & Sorbo 2010; Barnaby & Peloso 2011; Barnaby et al. 2011)

$$S \supset \int {\rm d}^4x\,\sqrt{-g}\left(-\frac{\alpha}{4f}\phi F^{\mu\nu}\tilde{F}_{\mu\nu}\right), \tag{114}$$

where $F_{\mu\nu} = \partial_\mu A_\nu - \partial_\nu A_\mu$, its dual is $\tilde{F}^{\mu\nu} = \epsilon^{\mu\nu\alpha\beta}F_{\alpha\beta}/2$, and α is a dimensionless constant which, from an effective field theory perspective, is expected to be of order one. For the potential of the axion field, we will not investigate further the consequences of the oscillatory part of the potential, focusing on the coupling of the axion field to the U(1) gauge field (effectively setting $\Lambda_0 = 0$).

The coupling of a pseudo-scalar axion with the gauge field has interesting phenomenological consequences, both for density perturbations and primordial gravitational waves (Barnaby & Peloso 2011; Sorbo 2011; Barnaby et al. 2011, 2012; Meerburg & Pajer 2013; Ferreira & Sloth 2014). Gauge field quanta source the axion field via an inverse decay process $\delta A + \delta A \rightarrow \delta\varphi$, modifying the usual predictions already at the power spectrum level. Additionally, the inverse decay can generate a high level of primordial NG.

The parameter

$$\xi = \frac{\alpha|\dot{\phi}|}{2fH} \tag{115}$$

characterizes the strength of the inverse decay effects. If $\xi < 1$ the coupling is too small to produce any modifications to the usual predictions of the uncoupled model. For previous constraints on ξ see Barnaby et al. (2011, 2012) and Meerburg & Pajer (2013). Using the slow-roll approximation and neglecting the small oscillatory part of the potential, one can express

$$\xi = M_{\rm Pl}\frac{\alpha}{f}\sqrt{\frac{p}{8N+2p}}, \tag{116}$$

where N is, as usual, the number of e-folds to the end of inflation. The scalar power spectrum of curvature perturbations is given by

$$\mathcal{P}_{\mathcal{R}}(k) = \mathcal{P}_*\left(\frac{k}{k_*}\right)^{n_{\rm s}-1}\left[1 + \mathcal{P}_*\left(\frac{k}{k_*}\right)^{n_{\rm s}-1} f_2(\xi(k))\, e^{4\pi\xi_*}\left(\frac{k}{k_*}\right)^{2\pi\xi_*\epsilon_2}\right], \tag{117}$$

where (Meerburg & Pajer 2013)

$$\xi(k) = \xi_*\left[1 + \frac{\epsilon_2}{2}\ln\left(\frac{k}{k_*}\right)\right]. \tag{118}$$

Here an asterisk indicates evaluation at the pivot scale, $k_* = 0.05\,{\rm Mpc}^{-1}$, and $\mathcal{P}_* = H_*^4/(4\pi^2\dot{\phi}_*^2)$ and $n_{\rm s} - 1 = -2\epsilon_1 - \epsilon_2$ are the amplitude and spectral index, respectively, of the standard slow-roll power spectrum of vacuum-mode curvature perturbations (the usual power spectrum in the absence of the gauge-coupling). By numerically evaluating the function $f_2(\xi)$ (defined in Eq. (3.27) of Barnaby et al. 2011), we created an analytical fit to this function accurate to better than 2% for $0.1 < \xi_* < 7$.[14] In the following, unless stated otherwise, we fix $p = 4/3$ as in the previous subsection and assume instantaneous reheating so that $N_* \approx 57.5$ and the slow-roll parameters ϵ_1 and ϵ_2 are fixed. For the tensor power spectrum we adopt the approximation (Barnaby et al. 2011)

$$\mathcal{P}_{\rm t}(k) = \mathcal{P}_{\rm t}\left(\frac{k}{k_*}\right)^{n_{\rm t}}\left[1 + \frac{\pi^2}{2}\mathcal{P}_{\rm t}f_{{\rm t},L}(\xi(k))e^{4\pi\xi_*}\left(\frac{k}{k_*}\right)^{n_{\rm t}+2\pi\epsilon_2\xi_*}\right], \tag{119}$$

[14] The fitting function used is $\exp\{-a - b\,\ln(\xi) - c\,[\ln(\xi)]^2 + {\rm d}[\ln(\xi)]^3 + e\,[\ln(\xi)]^4\}$, where the coefficients are $a = 10.8$, $b = 4.58$, $c = 0.51$, $d = 0.01$, and $e = 0.02$.

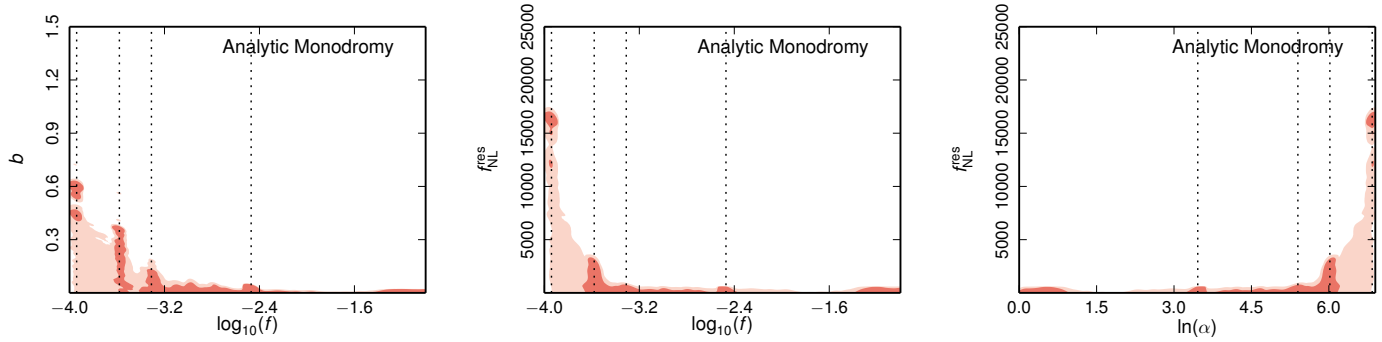

Fig. 42. Derived constraints on the parameters of the potential, Eq. (109), as well as the predicted resonant NG, $f_{\rm NL}^{\rm res}$, using the analytic template, showing joint 68% and 95% CL. The dotted lines mark the frequencies showing the highest-likelihood improvements (see text).

where

$$f_{{\rm t},L}(\xi(k)) = 2.6\times10^{-7}\xi^{-5.7}(k). \tag{120}$$

Here $\mathcal{P}_{\rm t} = 2H_*^2/(\pi^2 M_{\rm Pl}^2)$ and $n_{\rm t} = -2\epsilon_1$ are the "usual" expressions for the tensor amplitude and tensor tilt in standard slow-roll inflation.

The total bispectrum is (Barnaby et al. 2012)

$$B(k_i) = B_{\rm inv.dec.}(k_i) + B_{\rm res}(k_i) \tag{121a}$$

$$= f_{\rm NL}^{\rm inv.dec.}(\xi)\, F_{\rm inv.dec.}(k_i) + B_{\rm res}(k_i), \tag{121b}$$

where the explicit expression for $F_{\rm inv.dec.}(k_i)$ (Barnaby et al. 2011; see also Meerburg & Pajer 2013) is reported in Planck Collaboration XVII (2016). This shows that the inverse decay effects and the resonant effects (which arise from the oscillatory part of the potential) simply "add up" in the bispectrum. The nonlinearity parameter is

$$f_{\rm NL}^{\rm inv.dec.} = \frac{f_3(\xi_*)\mathcal{P}_*^3 e^{6\pi\xi_*}}{\mathcal{P}_{\mathcal{R}}^2(k_*)}. \tag{122}$$

The function $f_3(\xi_*)$ corresponds to the quantity $f_3(\xi_*;1,1)$ defined in Eq. (3.29) of Barnaby et al. (2011). We have computed $f_3(\xi_*)$ numerically and used a fit with an accuracy of better than 2%.[15] We use the observational constraint $f_{\rm NL}^{\rm inv.dec.} = 22.7 \pm 25.5$ (68% CL) obtained in Planck Collaboration XVII (2016) from an analysis where only the inverse decay type NG is assumed present. We omit the explicit expression for the resonant bispectrum $B_{\rm res}$, since it will not be used here.

We carried out an MCMC analysis of constraints on the (scalar and tensor) power spectra predicted by this model with the *Planck* TT+lowP likelihood, marginalizing over standard priors for the cosmological parameters and foreground parameters with the uniform priors $2.5 \le \ln[10^{10}\mathcal{P}_*] \le 3.7$ and $0.1 \le \xi_* \le 7.0$.

The power spectrum constraint gives

$$0.1 \le \xi_* \le 2.3 \quad (95\%\ {\rm CL}). \tag{123}$$

Given that $f_{\rm NL}^{\rm inv.dec.}$ is exponentially sensitive to ξ, this translates into the prediction (using Eq. (122)) $f_{\rm NL}^{\rm inv.dec.} \le 1.2$, which is significantly tighter than the current bispectrum constraint from Planck Collaboration XVII (2016). Indeed, importance sampling with the likelihood for $f_{\rm NL}^{\rm inv.dec.}$, taken to be a Gaussian centred on the NG estimate $f_{\rm NL}^{\rm inv.dec.} = 22.7 \pm 25.5$ (68% CL) (Planck Collaboration XVII 2016), changes the limit on ξ_* only at the second decimal place.

We now derive constraints on model parameters using only the observational constraint on $f_{\rm NL}^{\rm inv.dec.}$. The constraints thus derived are applicable for generic p and also to the axion monodromy model discussed in Sect. 10.3, even in the case $\Lambda_0 \neq 0$. We follow the procedure described in Sect. 11 of Planck Collaboration XVII (2016). The likelihood for $f_{\rm NL}^{\rm inv.dec.}$ is taken to be a Gaussian centred on the NG estimate $f_{\rm NL}^{\rm inv.dec.} = 22.7 \pm 25.5$ (68% CL) (Planck Collaboration XVII 2016). We use the expression of Eq. (122), where $f_3(\xi_*)$ is numerically evaluated. To find the posterior distribution for the parameter ξ_* we choose uniform priors in the intervals $1.5\times10^{-9} \le \mathcal{P}_* \le 3.0\times10^{-9}$ and $0.1 \le \xi_* \le 7.0$. This yields 95% CL constraints for ξ_* (for any value of p) of

$$\xi_* \le 2.5 \quad (95\%\ {\rm CL}). \tag{124}$$

If we choose a log-constant prior on ξ_* we find

$$\xi_* \le 2.2 \quad (95\%\ {\rm CL}). \tag{125}$$

For both cases the results are insensitive to the upper limit chosen for the prior on ξ_* since the likelihood quickly goes to zero for $\xi_* > 3$. As the likelihood for ξ_* is fairly flat, the tighter constraint seen for the log-constant case is mildly prior driven. The constraints from the bispectrum are consistent with, and slightly worse than, the result from the power spectrum alone.

Using a similar procedure and Eq. (116) one can also obtain a constraint on α/f. Adopting a log-constant prior[16] $2 \le \alpha/f \le 100$ and uniform priors $50 \le N_* \le 70$ and $1.5\times10^{-9} \le \mathcal{P}_* \le 3.0\times10^{-9}$ we obtain the 95% CL constraints

$$\alpha/f \le 48 M_{\rm Pl}^{-1} \ \text{ for } \ p=1, \qquad \alpha/f \le 35 M_{\rm Pl}^{-1} \ \text{ for } \ p=2, \tag{126}$$

and

$$\alpha/f \le 42 M_{\rm Pl}^{-1} \ \text{ for } \ p=4/3. \tag{127}$$

For example, for a linear potential, $p = 1$, if $\alpha \sim 1$ as suggested by effective field theory, then the axion decay constant f is constrained to be

$$f \ge 0.020 M_{\rm Pl} \quad (95\%\ {\rm CL}), \tag{128}$$

while for a potential with $p = 4/3$ we find

$$f \ge 0.023 M_{\rm Pl} \quad (95\%\ {\rm CL}). \tag{129}$$

These limits are complementary to those derived in Sect. 10.3.

[15] The fit has the same expression as the one for $f_2(\xi)$ with coefficients $a = 17.0048$, $b = 6.6578$, $c = 0.96479$, $d = 0.0506098$, and $e = 0.039139$.

[16] We give only the results for a log-constant prior on α/f, which is well-motivated since it corresponds to a log-constant prior on the axion decay constant for some fixed α.

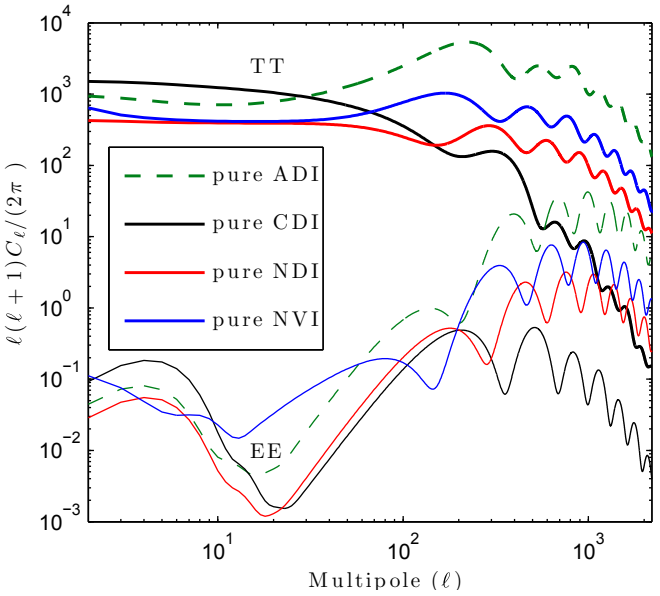

Fig. 43. Angular power spectra for the scale-invariant (i.e., $n_{\mathcal{RR}} = 1$) pure adiabatic mode (ADI, green dashed curves) and for the scale invariant ($n_{\mathcal{II}} = 1$) pure isocurvature (CDI, NDI, or NVI) modes, with equal primordial perturbation amplitudes. The thick lines represent the temperature auto-correlation (*TT*) and the thin lines the *E*-mode polarization auto-correlation (*EE*).

11. Constraints on isocurvature modes

In PCI13, we presented constraints on a number of simple models featuring a mixture of the adiabatic (ADI) mode and one type of isocurvature mode. We covered the cases of CDM density isocurvature (CDI), neutrino density isocurvature (NDI), and neutrino velocity isocurvature (NVI) modes (Bucher et al. 2000) with different assumptions concerning the correlation (Langlois 1999; Amendola et al. 2002) between the primordial adiabatic and isocurvature perturbations. Isocurvature modes, possibly correlated among themselves and with the adiabatic mode, can be generated in multi-field models of inflation; however, at present a mechanism for exciting the neutrino velocity isocurvature mode is lacking. Section 11.2 shows how these constraints have evolved with the new *Planck* TT+lowP likelihoods, how much including the *Planck* lensing likelihood changes the results, and what extra information the *Planck* high-ℓ polarization contributes. A pure isocurvature mode as a sole source of perturbations has been ruled out (Enqvist et al. 2002), since, as can be seen from Fig. 43, any of the isocurvature modes leads to an acoustic peak structure for the temperature angular power very different from the adiabatic mode, which fits the data very well. The different phases and tilts of the various modes also occur in the polarization spectra, as shown in Fig. 43 for the *E* mode.[17]

In Sect. 11.4 we add one extra degree of freedom to the generally-correlated ADI+CDI model by allowing primordial tensor perturbations (assuming the inflationary consistency relation for the tilt of the tensor power spectrum and its running). Our main goal is to explore a possible degeneracy between tensor modes and negatively-correlated CDI modes, tending to tilt the large-scale temperature spectrum in opposite directions. In Sect. 11.5, we update the constraints on three special cases motivated by axion or curvaton scenarios.

The goal of this analysis is to test the hypothesis of adiabaticity and establish the robustness of the base ΛCDM model against different assumptions concerning initial conditions (Sect. 11.3). Adiabaticity is also an important probe of the inflationary paradigm, since any significant detection of isocurvature modes would exclude the possibility that all perturbations in the Universe emerged from quantum fluctuations of a single inflaton field, which can excite only one degree of freedom, the curvature (i.e., adiabatic) perturbation.[18]

In this section, theoretical predictions were obtained with a modified version of the `CAMB` code (version `Jul14`) while parameter exploration was performed with the `MultiNest` nested sampling algorithm.

11.1. Parameterization and notation

A general mixture of the adiabatic mode and one isocurvature mode is described by the three functions $\mathcal{P}_{\mathcal{RR}}(k)$, $\mathcal{P}_{\mathcal{II}}(k)$, and $\mathcal{P}_{\mathcal{RI}}(k)$ describing the curvature, isocurvature, and cross-correlation power spectra, respectively. Our sign conventions are such that positive values for $\mathcal{P}_{\mathcal{RI}}$ correspond to a positive contribution of the cross-correlation term to the Sachs-Wolfe component of the total temperature spectrum.

As in PCI13, we specify the amplitudes at two scales $k_1 < k_2$ and assume power-law behaviour, so that

$$\mathcal{P}_{\rm ab}(k) = \exp\left[\left(\frac{\ln(k)-\ln(k_2)}{\ln(k_1)-\ln(k_2)}\right)\ln\left(\mathcal{P}^{(1)}_{\rm ab}\right) + \left(\frac{\ln(k)-\ln(k_1)}{\ln(k_2)-\ln(k_1)}\right)\ln\left(\mathcal{P}^{(2)}_{\rm ab}\right)\right], \quad (130)$$

where $a, b = \mathcal{I}, \mathcal{R}$ and $\mathcal{I} = \mathcal{I}_{\rm CDI}$, $\mathcal{I}_{\rm NDI}$, or $\mathcal{I}_{\rm NVI}$. We set $k_1 = 0.002\,{\rm Mpc}^{-1}$ and $k_2 = 0.100\,{\rm Mpc}^{-1}$, so that $[k_1, k_2]$ spans most of the range constrained by the *Planck* data. The positive definiteness of the initial condition matrix imposes a constraint on its elements at any value of k:

$$[\mathcal{P}_{\rm ab}(k)]^2 \le \mathcal{P}_{\rm aa}(k)\mathcal{P}_{\rm bb}(k). \quad (131)$$

[17] The transfer function mapping the primordial CDI mode to $C_\ell^{\rm TT}$ is suppressed by a factor $(k/k_{\rm eq})^{-2} \sim (\ell/\ell_{\rm eq})^{-2}$ relative to the ADI mode, where $k_{\rm eq}$ is the wavenumber of matter-radiation equality. As seen in Fig. 43, there is a similar damping for the *E* mode in the CDI versus the ADI case. Therefore, to be observable at high ℓ, a CDI mode should be (highly) blue tilted. So, if the data favoured as small as possible a disturbance by CDI over all scales, then the CDI should have a spectral index, $n_{\mathcal{II}}$, of roughly three. In practice, the lowest-ℓ part of the data has very little weight due to cosmic variance, and thus we expect that the data should favour $n_{\mathcal{II}}$ less than three, but significantly larger than one. This should be kept in mind when interpreting the results in the CDI case, i.e., one cannot expect strong constraints on the *primordial* CDI fraction at small scales, even if the data are purely adiabatic. The imprint of the baryon density isocurvature (BDI) mode in the CMB, at least at linear order, is indistinguishable from the CDI case, and hence we do not consider it separately as it can be described by $\mathcal{I}^{\rm effective}_{\rm CDI} = \mathcal{I}_{\rm CDI} + (\Omega_{\rm b}/\Omega_{\rm c})\mathcal{I}_{\rm BDI}$. The trispectrum, however, can in principle be used to distinguish the BDI and CDI modes (Grin et al. 2014).

[18] However, conversely, if no isocurvature was detected, the fluctuations could have been seeded either by single- or multi-field inflation, since later processes easily wash out inflationary isocurvature perturbations (Mollerach 1990; Weinberg 2004; Beltrán et al. 2005). An example is the curvaton model, in which perturbations can be purely isocurvature at Hubble exit during inflation, but are later converted to ADI if the curvaton or curvaton particles (Linde & Mukhanov 2006) dominate the energy density at the curvaton's decay. For a summary of various curvaton scenarios, see, e.g., Gordon & Lewis (2003).

We take uniform priors on the positive amplitudes,

$$\mathcal{P}^{(1)}_{\mathcal{RR}}, \mathcal{P}^{(2)}_{\mathcal{RR}} \in (10^{-9},\, 10^{-8}), \tag{132}$$

$$\mathcal{P}^{(1)}_{\mathcal{II}}, \mathcal{P}^{(2)}_{\mathcal{II}} \in (0,\, 10^{-8}). \tag{133}$$

The correlation spectrum can be positive or negative. For $a \neq b$ we apply a uniform prior at large scales (at k_1):

$$\mathcal{P}^{(1)}_{\rm ab} \in (-10^{-8},\, 10^{-8}), \tag{134}$$

but reject all parameter combinations violating the constraint in Eq. (131). To ensure that Eq. (131) holds for all k, we restrict ourselves to a scale-independent correlation fraction:

$$\cos\Delta_{\rm ab} \equiv \frac{\mathcal{P}_{\rm ab}}{(\mathcal{P}_{\rm aa}\mathcal{P}_{\rm bb})^{1/2}} \in (-1, 1). \tag{135}$$

Thus $\mathcal{P}^{(2)}_{\rm ab}$ is a derived parameter[19] given by

$$\mathcal{P}^{(2)}_{\rm ab} = \mathcal{P}^{(1)}_{\rm ab} \frac{\left(\mathcal{P}^{(2)}_{\rm aa}\mathcal{P}^{(2)}_{\rm bb}\right)^{1/2}}{\left(\mathcal{P}^{(1)}_{\rm aa}\mathcal{P}^{(1)}_{\rm bb}\right)^{1/2}}, \tag{136}$$

which in terms of spectral indices is equivalent to

$$n_{\rm ab} = \frac{1}{2}(n_{\rm aa} + n_{\rm bb}). \tag{137}$$

The conservative baseline likelihood is *Planck* TT+lowP. The results obtained with *Planck* TT, TE, EE+lowP should be interpreted with caution because the data used in the 2015 release are known to contain some low level systematics, in particular arising from T-to-E leakage, and it is possible that such systematics may be fit by the isocurvature auto-correlation and cross-correlation templates. (See Planck Collaboration XIII 2016 for a detailed discussion.)

In what follows, we quote our results in terms of derived parameters identical to those in PCI13. We define the primordial isocurvature fraction as

$$\beta_{\rm iso}(k) = \frac{\mathcal{P}_{\mathcal{II}}(k)}{\mathcal{P}_{\mathcal{RR}}(k) + \mathcal{P}_{\mathcal{II}}(k)}. \tag{138}$$

Unlike the primordial correlation fraction $\cos\Delta$ defined in Eq. (135), $\beta_{\rm iso}$ is scale-dependent in the general case. We present bounds on this quantity at $k_{\rm low} = k_1$, $k_{\rm mid} = 0.050\,{\rm Mpc}^{-1}$, and $k_{\rm high} = k_2$.

We report constraints on the relative adiabatic (ab = $\mathcal{RR}$), isocurvature (ab = $\mathcal{II}$), and correlation (ab = $\mathcal{RI}$) components according to their contribution to the observed CMB temperature variance in various multipole ranges:

$$\alpha_{\rm ab}(\ell_{\rm min}, \ell_{\rm max}) \equiv \frac{(\Delta T)^2_{\rm ab}(\ell_{\rm min}, \ell_{\rm max})}{(\Delta T)^2_{\rm tot}(\ell_{\rm min}, \ell_{\rm max})}, \tag{139}$$

where

$$(\Delta T)^2_{\rm ab}(\ell_{\rm min}, \ell_{\rm max}) = \sum_{\ell=\ell_{\rm min}}^{\ell_{\rm max}} (2\ell+1) C^{\rm TT}_{{\rm ab},\ell}. \tag{140}$$

The ranges considered are $(\ell_{\rm min}, \ell_{\rm max}) = (2, 20)$, $(21, 200)$, $(201, 2500)$, and $(2, 2500)$, where the last range describes the total contribution to the observed CMB temperature variance. Here $\alpha_{\mathcal{RR}}$ measures the adiabaticity of the temperature angular power spectrum, a value of unity meaning "fully adiabatic initial conditions". Values less than unity mean that some of the observed power comes from the isocurvature or correlation spectrum, while values larger than unity mean that some of the power is "cancelled" by a negatively-correlated isocurvature contribution. The relative non-adiabatic contribution can be expressed as $\alpha_{\rm non\text{-}adi} \equiv 1 - \alpha_{\mathcal{RR}} = \alpha_{\mathcal{II}} + \alpha_{\mathcal{RI}}$.

11.2. Results for generally-correlated adiabatic and one isocurvature mode (CDI, NDI, or NVI)

Results are reported as 2D and 1D marginalized posterior probability distributions. Numerical 95% CL intervals or upper bounds are tabulated in Table 16.

Figure 44 shows the *Planck* 68% and 95% CL contours for various 2D combinations of the primordial adiabatic and isocurvature amplitude parameters at large scales ($k_1 = 0.002\,{\rm Mpc}^{-1}$) and small scales ($k_2 = 0.100\,{\rm Mpc}^{-1}$) for (a) the generally-correlated ADI+CDI; (b) ADI+NDI; and (c) ADI+NVI models. Overall, the results using *Planck* TT+lowP are consistent with the nominal mission results in PCI13, but slightly tighter. In the first panels of Figs. 44a–c we also show the constraints on the curvature perturbation power in the pure adiabatic case. Comparing the generally-correlated isocurvature case to the pure adiabatic case with the same data combination summarizes neatly what the data tell us about the initial conditions. If the contours in the $\mathcal{P}^{(1)}_{\mathcal{RR}}$-$\mathcal{P}^{(2)}_{\mathcal{RR}}$ plane were shifted significantly relative to the pure adiabatic case, the missing power could come either from the isocurvature and postive correlation contributions, or the extra adiabatic power could be cancelled by a negative correlation contribution. We can see that these shifts are small. The low-ℓ temperature data continue to mildly favour a negative correlation (see in particular the bottom middle panel for each of the three models), since compared to the prediction of the best-fit adiabatic base ΛCDM model, the TT angular power at multipoles $\ell \lesssim 40$ is somewhat low. But the dotted grey shaded contours in the three middle top panels show that for *Planck* TT+lowP, the posterior peaks at values $(\mathcal{P}^{(1)}_{\mathcal{II}}, \mathcal{P}^{(2)}_{\mathcal{II}})$ entirely consistent with (0, 0), i.e., the pure adiabatic case is preferred. The best-fit values of $(\mathcal{P}^{(1)}_{\mathcal{II}}, \mathcal{P}^{(2)}_{\mathcal{II}})$ are $(1.4\times10^{-11}, 4.7\times10^{-13})$ for CDI, $(1.2\times10^{-12}, 4.6\times10^{-10})$ for NDI, and $(1.6\times10^{-12}, 2.3\times10^{-10})$ for NVI, while $(\mathcal{P}^{(1)}_{\mathcal{RR}}, \mathcal{P}^{(2)}_{\mathcal{RR}}) \approx (2.4\times10^{-9}, 2.1\times10^{-9})$. It may appear from the bottom-centre panels of Fig. 44 that there is nonzero posterior probability for $\mathcal{P}^{(1)}_{\mathcal{RI}} \neq 0$ when $\mathcal{P}^{(1)}_{\mathcal{II}} = 0$, which would violate the positivity constraint, Eq. (131). However, the leftmost pixels of the plots are actually evaluated at values of $\mathcal{P}^{(1)}_{\mathcal{II}}$ large enough that the constraint is satisfied.

Including the *Planck* lensing likelihood does not significantly affect the non-adiabatic primordial powers, except for tightening the constraints on the adiabatic power (see the blue versus black contours in the first panels of Figs. 44a–c). Including the lensing ($C^{\phi\phi}_\ell$) likelihood constrains the optical

[19] Given our ansatz of power-law primordial spectra, if we treated $\mathcal{P}^{(2)}_{\rm ab}$ as an independent parameter as we do with $\mathcal{P}^{(1)}_{\rm ab}$, Eq. (131) would always be violated somewhere outside $[k_1, k_2]$. In PCI13, we dealt with this by assuming that when maximal (anti-)correlation is reached at some scale, the correlation remains at (−)100% beyond this scale. This introduced a kink in the cross-correlation spectrum, located at a different wavenumber for each model. Even though the range $[k_1, k_2]$ was chosen to span most of the observable scales, this kink tended to impact the smallest (or largest) multipole values used in the analysis. In particular, the kink helped fit the dip in the temperature angular power in the multipole range $\ell \approx$ 10–40.

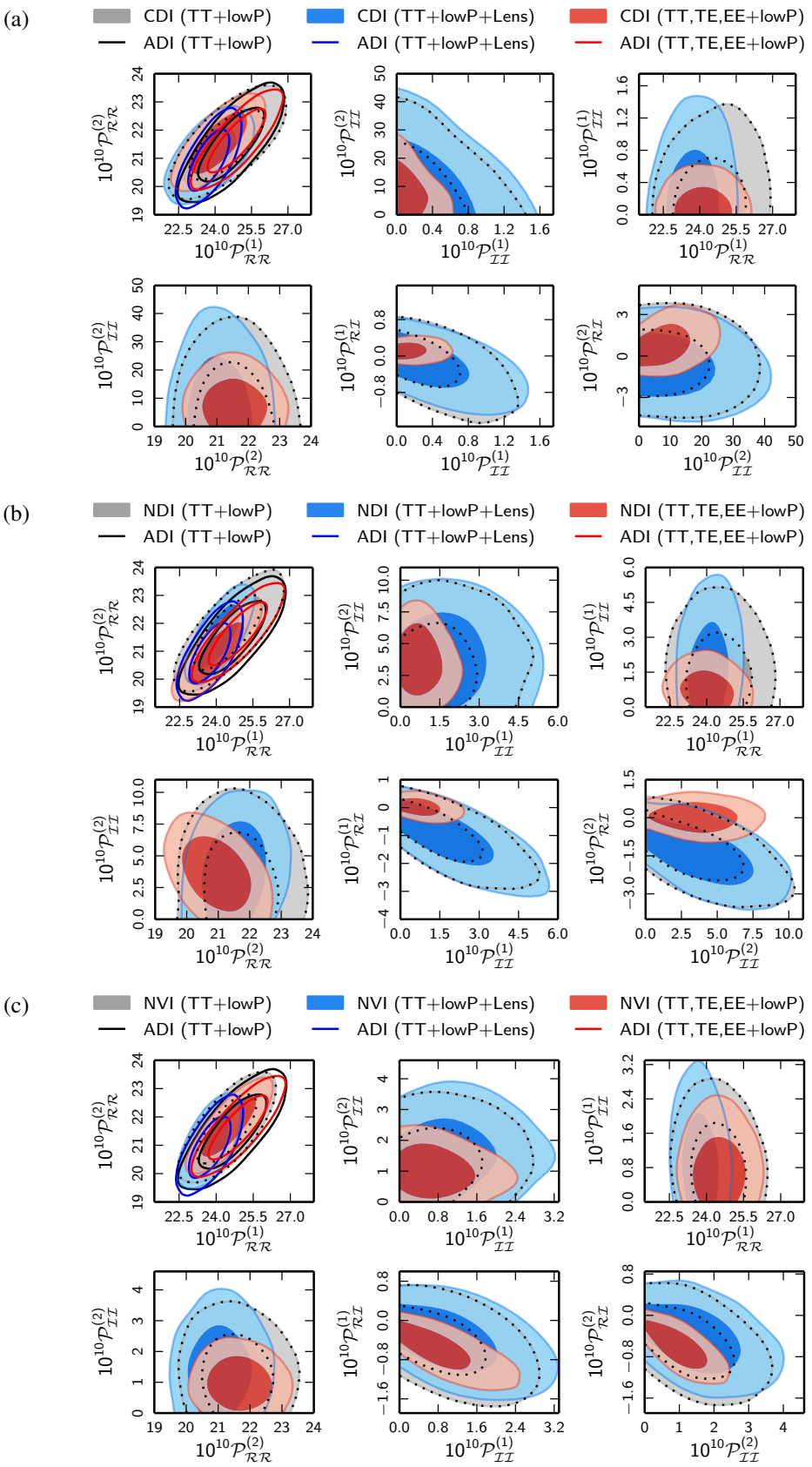

Fig. 44. 68% and 95% CL constraints on the primordial perturbation power in general mixed ADI+CDI **a)**; ADI+NDI **b)**; and ADI+NVI **c)** models at two scales, $k_1 = 0.002\,\mathrm{Mpc}^{-1}$ (1) and $k_2 = 0.100\,\mathrm{Mpc}^{-1}$ (2), for *Planck* TT+lowP (grey regions highlighted by dotted contours), *Planck* TT+lowP+lensing (blue), and *Planck* TT, TE, EE+lowP (red). *In the first panels*, we also show contours for the pure adiabatic base ΛCDM model with the corresponding colours of solid lines.

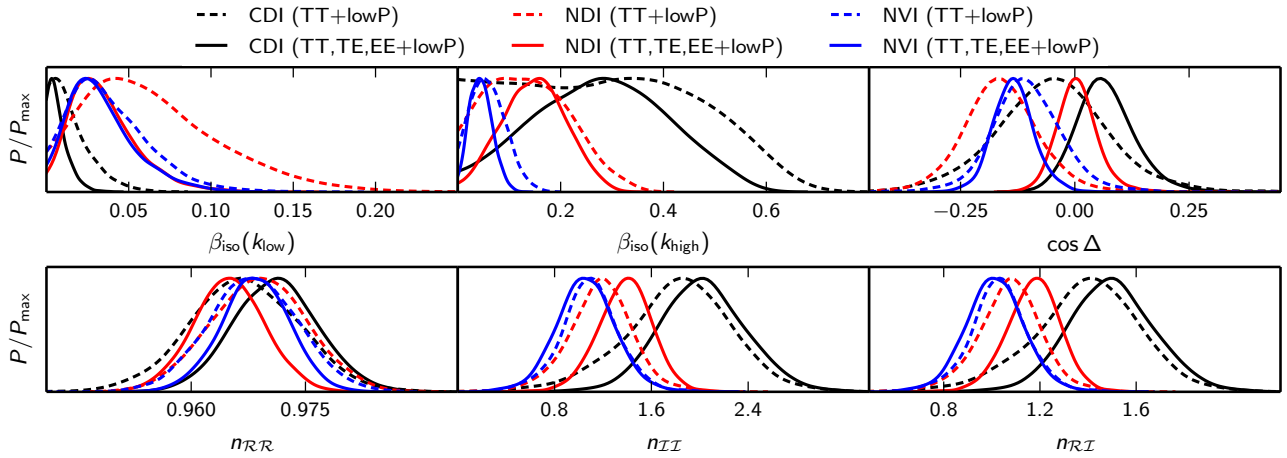

Fig. 45. Constraints on the primordial isocurvature fraction, $\beta_{\rm iso}$, at $k_{\rm low} = 0.002\,{\rm Mpc}^{-1}$ and $k_{\rm high} = 0.100\,{\rm Mpc}^{-1}$, the primordial correlation fraction, $\cos\Delta$, the adiabatic spectral index, $n_{\mathcal{RR}}$, the isocurvature spectral index, $n_{\mathcal{II}}$, and the correlation spectral index, $n_{\mathcal{RI}} = (n_{\mathcal{RR}} + n_{\mathcal{II}})/2$, with *Planck* TT+lowP data (dashed curves) and TT, TE, EE+lowP data (solid curves), for the generally-correlated mixed ADI+CDI (black), ADI+NDI (red), and ADI+NVI (blue) models. All these parameters are derived, and the distributions shown here result from a uniform prior on the primary parameters, as detailed in Eqs. (132)–(134). However, the effect of the non-flat derived-parameter priors is negligible for all parameters except for $n_{\mathcal{II}}$ (and $n_{\mathcal{RI}}$) where the prior biases the distribution toward one. With TT+lowP, the flatness of $\beta_{\rm iso}(k_{\rm high})$ in the CDI case up to a "threshold" value of about 0.5 is a consequence of the $(k/k_{\rm eq})^{-2}$ damping of its transfer function as explained in Footnote 17.

depth τ more tightly than the high-ℓ temperature and low-ℓ polarization alone (Planck Collaboration XIII 2016). As there is a strong degeneracy between τ and the primordial (adiabatic) perturbation power $\mathcal{P}_{\mathcal{RR}}$ (denoted in the other sections of this paper by $A_{\rm s}$), it is natural that adding the lensing data leads to stronger constraints on $\mathcal{P}_{\mathcal{RR}}$. Moreover, replacing the low-ℓ likelihood *Planck* lowP by *Planck* lowP+WP constrains τ better (Planck Collaboration XIII 2016). In the ADI+CDI case the effect of this replacement was very similar to adding the *Planck* lensing data (see also Table 16). Although the *Planck* lensing data do not directly constrain the isocurvature contribution,[20] they can shift and tighten the constraints on some derived isocurvature parameters by affecting the favoured values of the standard parameters (present even in the pure adiabatic model). However this effect is small as confirmed in Table 16. Therefore, in the figures we do not show 1D posteriors of the derived isocurvature parameters for *Planck* TT+lowP+lensing, since they would be (almost) indistinguishable from *Planck* TT+lowP, as we see in Fig. 44 for the primary non-adiabatic parameters.

In contrast, the high-ℓ *polarization* data significantly tighten the bounds on isocurvature and cross-correlation parameters, as seen by comparing the dotted grey and red contours in Fig. 44. The significant negative correlation previously allowed by the temperature data in the ADI+CDI and ADI+NDI models is now disfavoured. This is also clearly visible in the 1D posteriors of primordial and observable isocurvature and cross-correlation fractions shown, respectively, in Figs. 45 and 46. Note how the $\cos\Delta$ and $\alpha_{\mathcal{RI}}$ parameters are driven towards zero by the inclusion of the high-ℓ TE, EE data (from the dashed to the solid lines) in the ADI+CDI and ADI+NDI cases. We also observed that when the lowP data are replaced by a simple Gaussian prior on the reionization optical depth ($\tau = 0.078 \pm 0.019$), the trend is similar. The high-ℓ ($\ell \geq 30$) *Planck* TT data allow a large negative correlation, while the high-ℓ *Planck* TE, EE data prefer positive correlation. This is clearly seen in Fig. 47 for the ADI+CDI case. The best-fit values show an even more dramatic effect. We find $\cos\Delta = -0.55$ with TT+lowP, and +0.15 with TT, TE, EE+lowP.

Hence there is a competition between the temperature and polarization data that balances out and yields almost symmetric results about zero correlation (except in the ADI+NVI case). The isocurvature auto-correlation amplitude is also strongly reduced, especially in the ADI+CDI case. The best-fit values are slightly offset from $(\mathcal{P}^{(1)}_{\mathcal{II}}, \mathcal{P}^{(2)}_{\mathcal{II}}) = (0, 0)$, but the pure adiabatic model still lies inside the 68% CL (for ADI+CDI and ADI+NDI) or 95% CL (for ADI+NVI) regions. In summary, the high-ℓ polarization data exhibit a strong preference for adiabaticity, although one should keep in mind the possibility of unaccounted systematic effects in the polarization data, possibly leading to artificially strong constraints. For example, the tendency for polarization to shift the constraints towards positive correlation may be due to particular systematic effects that mimic modified acoustic peak structure, as we discussed in Sect. 11.1.

We also performed a parameter extraction with the *Planck* TT, TE, EE+lowP+lensing data, but this combination did not provide interesting new constraints. We found only a tightening of bounds on the standard adiabatic parameters as in the *Planck* TT+lowP+lensing case.

We provide 95% CL upper limits or ranges for $\beta_{\rm iso}$, $\cos\Delta$, and $\alpha_{\mathcal{RR}}$ in Table 16. With *Planck* TT+lowP, the constraints on the non-adiabatic contribution to the temperature variance, $1 - \alpha_{\mathcal{RR}}(2, 2500)$, are $(-1.5\%, 1.9\%)$, $(-4.0\%, 1.4\%)$, and $(-2.3\%, 2.4\%)$ in the ADI+CDI, ADI+NDI, and ADI+NVI cases, respectively.[21] With *Planck* TT, TE, EE+lowP these tighten to $(0.1\%, 1.5\%)$, $(-0.1\%, 2.2\%)$, and $(-2.0\%, 0.8\%)$. In the ADI+CDI case, zero is not in the 95% CL interval, but this should not be considered a detection of non-adiabaticity. For example, as mentioned above, $(\mathcal{P}^{(1)}_{\mathcal{II}}, \mathcal{P}^{(2)}_{\mathcal{II}}) = (0, 0)$ is in the 68% CL region, and the best-fit values are $(\mathcal{P}^{(1)}_{\mathcal{II}}, \mathcal{P}^{(2)}_{\mathcal{II}}) = (1.0 \times 10^{-13}, 3.5 \times 10^{-9})$. Moreover,

[20] This is expected, since already with *Planck* TT+lowP, the allowed isocurvature fraction is so small that it hardly affects the lensing potential spectrum, $C^{\phi\phi}_{\ell}$.

[21] These numbers can be positive even if the correlation contribution is negative. This happens whenever $\alpha_{\mathcal{II}} > |\alpha_{\mathcal{RI}}|$. Thus in the observational non-adiabaticity estimator $1 - \alpha_{\mathcal{RR}}(2, 2500)$, the negative numbers are not as pronounced as in the primordial correlation fraction $\cos\Delta$.

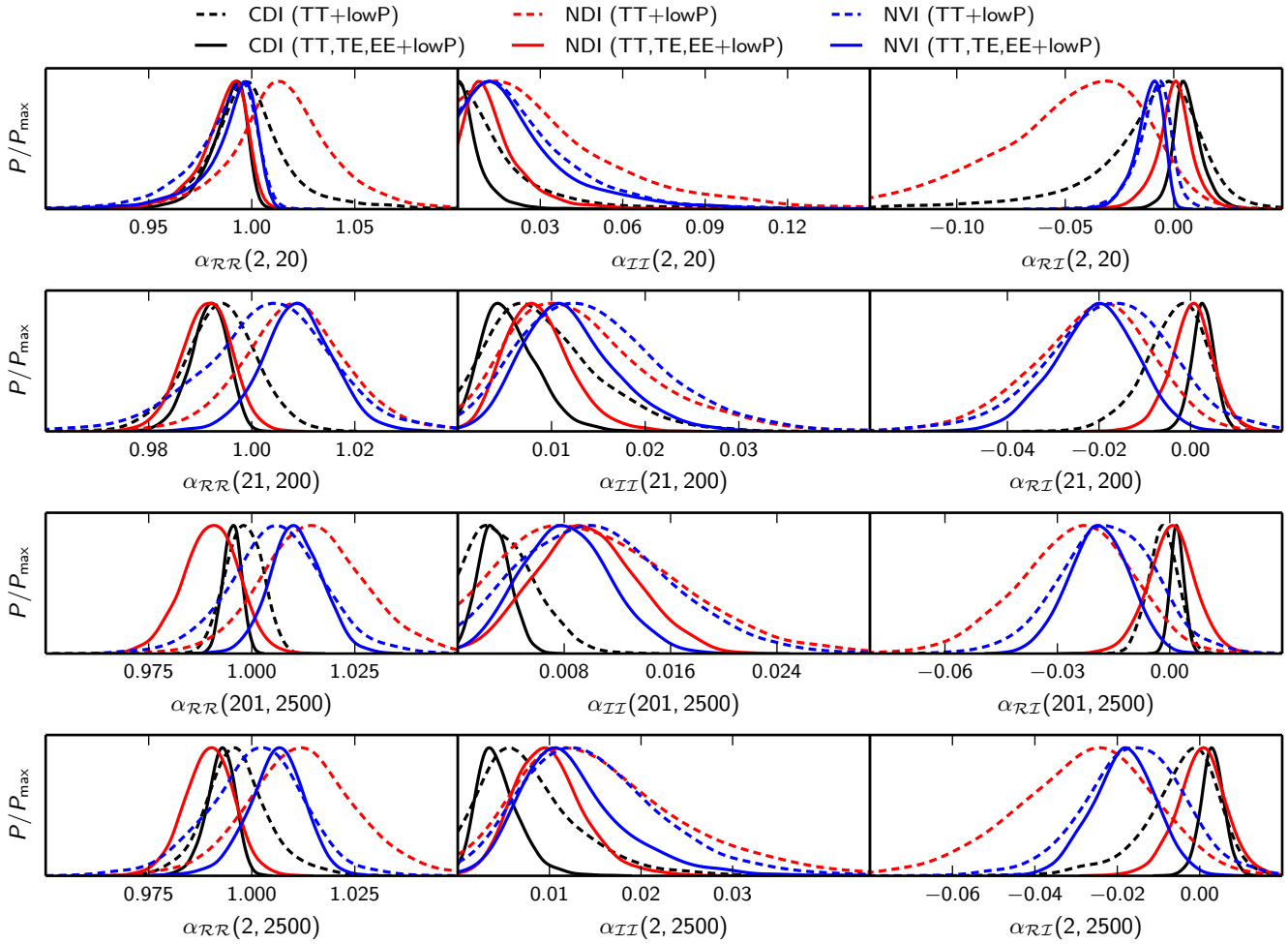

Fig. 46. Constraints on the fractional contribution of the adiabatic ($\mathcal{RR}$), isocurvature ($\mathcal{II}$), and correlation ($\mathcal{RI}$) components to the CMB temperature variance in various multipole ranges, as defined in Eq. (139), with *Planck* TT+lowP data (dashed curves) and with *Planck* TT, TE, EE+lowP data (solid curves). These are shown for the generally-correlated mixed ADI+CDI (black), ADI+NDI (red), or ADI+NVI (blue) models.

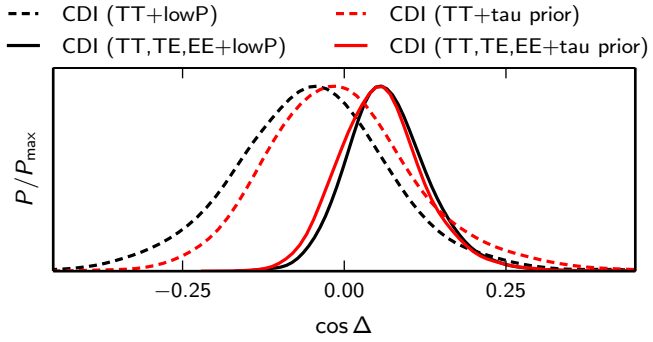

Fig. 47. Constraints on the primordial correlation fraction, $\cos\Delta$, in the mixed ADI+CDI model with *Planck* TT+lowP data (dashed black curve) compared to the case where *Planck* lowP data are not used, but replaced by a Gaussian prior $\tau = 0.078 \pm 0.019$ (dashed red curve). The same exercise is repeated with *Planck* TT, TE, EE data (solid curves) demonstrating that to a great extent the preferred value of $\cos\Delta$ is driven by the high-ℓ data.

the improvement in χ^2 with respect to the adiabatic model is only 5.3 with 3 extra parameters, so this is not a significant improvement of fit. Indeed, for all generally-correlated mixed models the improvement in χ^2 is very small. In particular, with *Planck* TT+lowP it does not even exceed the number of extra degrees of freedom, which is three (see Table 16).

Finally, we checked whether there is any Bayesian evidence for the presence of generally-correlated adiabatic and isocurvature modes. In all cases and with all data combinations studied, the Bayesian model comparison supports the null hypothesis, i.e., adiabaticity. Indeed, the logarithm of the evidence ratio is $\ln B = \ln(P_{\rm ISO}/P_{\rm ADI}) < -5$ (i.e., odds of much greater than 150:1 in favour of pure adiabaticity within *Planck*'s accuracy and given the parameterization and prior ranges used in our analysis), except for ADI+NDI with *Planck* TT+lowP+lensing, for which the evidence ratio is slightly larger, −4.6, corresponding to odds of 1:100 for the ADI+NDI model compared to the pure adiabatic model.

11.3. Robustness of the determination of standard cosmological parameters

Another outcome of our analysis is the robustness of the determination of the standard cosmological parameters against assumptions on initial conditions. Figure 48 shows the 1D marginalized posteriors for several cosmological parameters (not all independent of each other) with the *Planck* TT+lowP data alone. For the first time, we observe that in the presence of

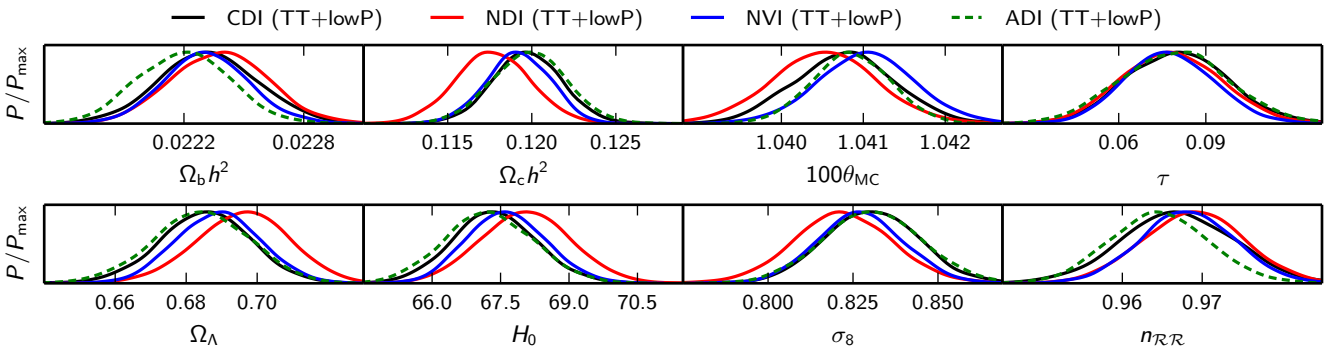

Fig. 48. Constraints on selected "standard" cosmological parameters with *Planck* TT+lowP data for the generally-correlated ADI+CDI (black), ADI+NDI (red), and ADI+NVI (blue) models compared to the pure adiabatic case (ADI, green dashed curves).

one generally-correlated isocurvature mode (CDI, NDI, or NVI), predictions for these parameters remain very stable with respect to the pure adiabatic case. Except for the ADI+NDI case, the posteriors neither broaden nor shift significantly. A small broadening is only observed in the sound horizon angle $\theta_{\rm MC}$, which is naturally the most sensitive parameter to tiny disturbances of the acoustic peak structure. In the ADI+NDI case, the peak of the posterior distribution for some parameters shifts slightly, but the largest shift (for $\Omega_{\rm c}h^2$) is less than 1σ.

It is striking that a scale-invariant adiabatic spectrum ($n_{\mathcal{RR}} = 1$) is excluded at many σ even when isocurvature modes are allowed: at 4.7σ (ADI+CDI), 5.0σ (ADI+NDI), and 5.4σ (ADI+NVI). This illustrates how much the constraining power of the CMB has improved. With WMAP data, there was still a strong degeneracy between, for example, the primordial isocurvature fraction and the adiabatic spectral index (Valiviita & Giannantonio 2009; Savelainen et al. 2013). This degeneracy nearly disappears with *Planck* TT+lowP, and even more so with *Planck* TT, TE, EE+lowP, as shown in the upper panel of Fig. 49. Contours in the ($n_{\mathcal{RR}}$, $\cos\Delta$) space also shrink considerably, with some correlation remaining between these parameters in the ADI+CDI and ADI+NVI cases (Fig. 49, lower panel).

11.4. CDI and primordial tensor perturbations

A primordial tensor contribution adds extra temperature angular power at low multipoles, where the adiabatic base ΛCDM model predicts slightly more power than seen in the data. Hence allowing for a nonzero tensor-to-scalar ratio r might tighten the constraints on positively-correlated isocurvature, but degrade them in negatively-correlated models. We test how treating r as a free parameter affects the constraints on isocurvature and how allowing for the generally-correlated CDI mode affects the constraints on r. These cases are denoted as "CDI+r". For comparison, we examine the pure adiabatic case in the same parameterization, and call it "ADI+r". We also consider another approach where we fix $r = 0.1$. These cases are named "CDI+$r = 0.1$" and "ADI+$r = 0.1$".

In the pure adiabatic case (where the curvature and tensor perturbations stay constant on super-Hubble scales), the primordial r is the same as the tensor-to-scalar ratio at the Hubble radius exit of perturbations during inflation, which we call $\tilde{r}$. However, in the presence of an isocurvature component, $\mathcal{P}_{\mathcal{RR}}$ is not constant in time even on super-Hubble scales (García-Bellido & Wands 1996). Instead, the isocurvature component may source $\mathcal{P}_{\mathcal{RR}}$, for example if the background trajectory in the field space is curved between Hubble exit and the end of inflation (Langlois 1999; Langlois & Riazuelo 2000; Gordon et al. 2001; Amendola et al. 2002). As a result, we will have at the primordial time

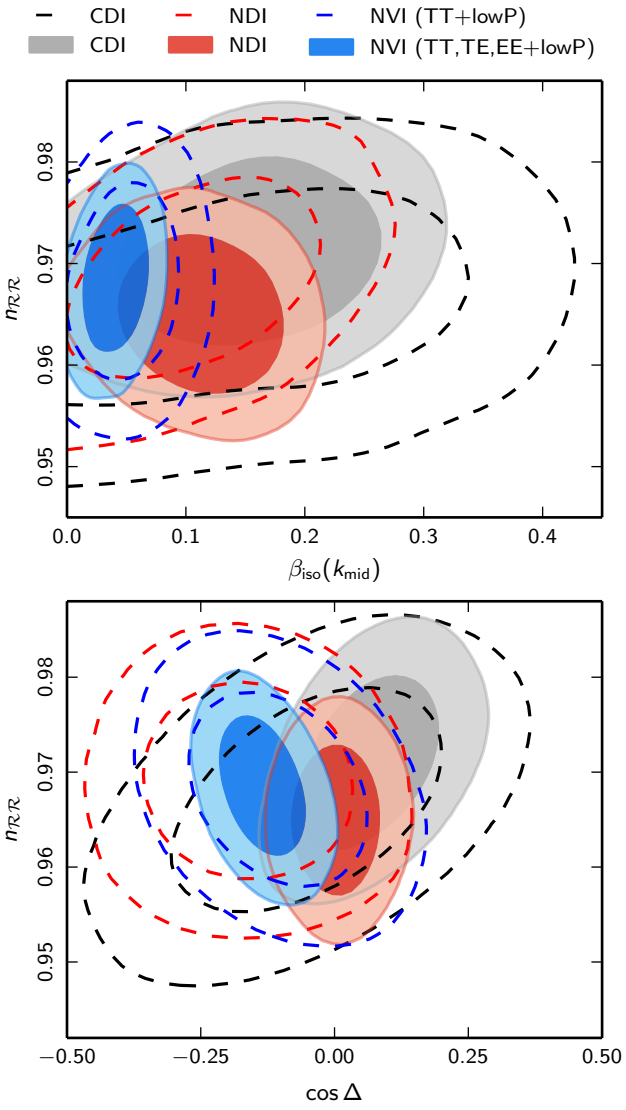

Fig. 49. Dependence of the determination of the adiabatic spectral index $n_{\mathcal{RR}}$ (called $n_{\rm s}$ in the other sections of this paper) on the primordial isocurvature fraction $\beta_{\rm iso}$ and correlation fraction $\cos\Delta$, with *Planck* TT+lowP data (dashed contours) and with *Planck* TT, TE, EE+lowP data (shaded regions).

$\mathcal{P}_{\mathcal{RR}} = \tilde{\mathcal{P}}_{\mathcal{RR}}/(1-\cos^2\Delta)$, where $\tilde{\mathcal{P}}_{\mathcal{RR}}$ is the curvature power at Hubble exit. That is, by the primordial time the curvature perturbation power is larger than at the Hubble radius exit time